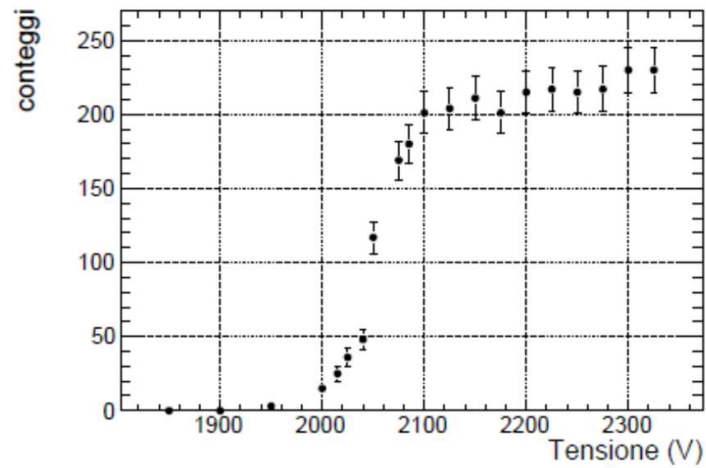
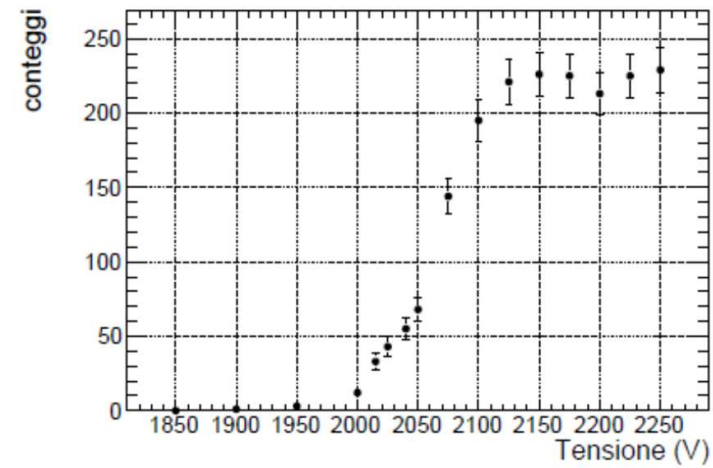


Integral pulse height distribution (curva di conteggio)



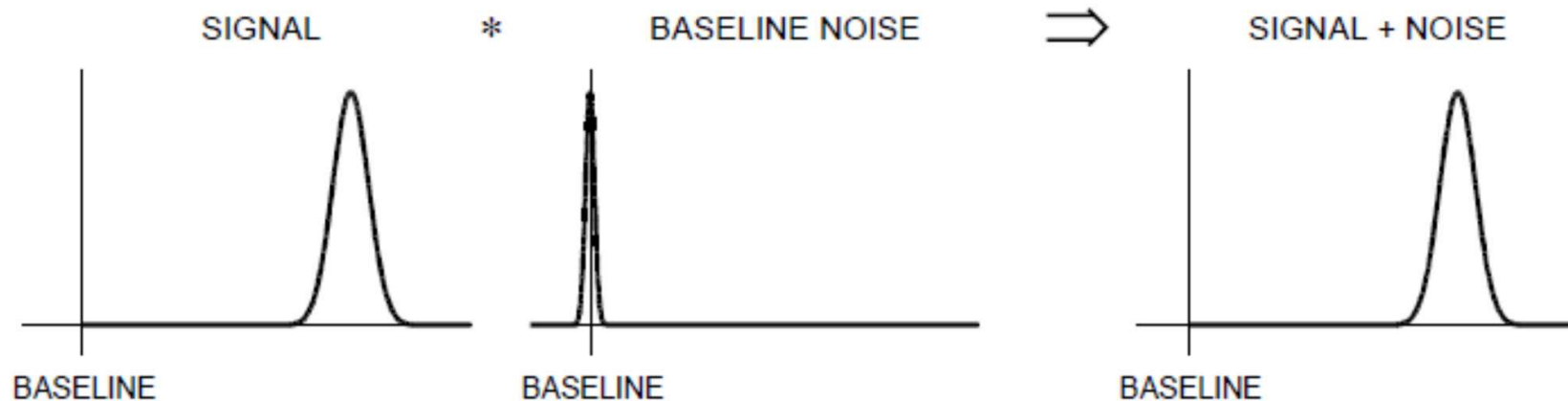
(a) PMT 2, soglia a 40 mV



(b) PMT 2, soglia a 45 mV

What determines Resolution?

Signal Variance \gg Baseline Variance



\Rightarrow Electronic (baseline) noise not important

Examples: • High-gain proportional chambers

• Scintillation Counters with High-Gain PMTs

e.g. 1 MeV γ -rays absorbed by NaI(Tl) crystal

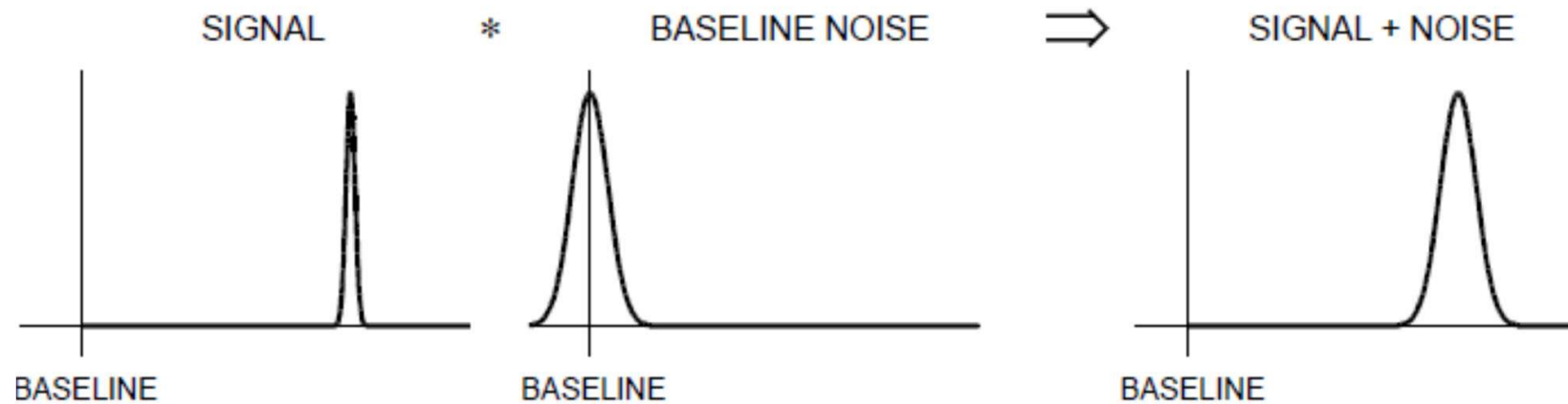
Number of photoelectrons: $N_{pe} \approx 8 \cdot 10^4 [\text{MeV}^{-1}] \times E_\gamma \times QE \approx 2.4 \cdot 10^4$

Variance typically: $\sigma_{pe} = N_{pe}^{1/2} \approx 160$ and $\sigma_{pe} / N_{pe} \approx 5 - 8\%$

Signal at PMT anode (assume Gain = 10^4): $Q_{sig} = G_{PMT} N_{pe} \approx 2.4 \cdot 10^8$ el and
 $\sigma_{sig} = G_{PMT} \sigma_{pe} \approx 1.2 \cdot 10^7$ el

whereas electronic noise easily $< 10^4$ el

Signal Variance \ll Baseline Variance



\Rightarrow Electronic (baseline) noise critical for resolution

- Examples:
- Gaseous ionization chambers (no internal gain)
 - Semiconductor detectors

e.g. in Si : Number of electron-hole pairs $N_{ep} = \frac{E_{dep}}{3.6 \text{ eV}}$

Variance $\sigma_{ep} = \sqrt{F \cdot N_{ep}}$ (where F = Fano factor ≈ 0.1)

For 50 keV photons: $\sigma_{ep} \approx 40 \text{ el} \Rightarrow \sigma_{ep} / N_{ep} = 7.5 \cdot 10^{-4}$

Obtainable noise levels are 10 to 1000 el.

Baseline fluctuations can have many origins ...

pickup of external interference

artifacts due to imperfect electronics

... etc.,

but the (practical) fundamental limit is electronic noise.

1.10 Detection limits and resolution

In addition to signal fluctuations originating in the sensor, the minimum detection limit and energy resolution are subject to fluctuations introduced by the electronics. The gain can be controlled very precisely, but electronic noise introduces baseline fluctuations, which are superimposed on the signal and alter the peak amplitude. Figure 1.24 (left) shows a typical noise waveform. Both the amplitude and time distributions are random.

When superimposed on a signal, the noise alters both the amplitude and time dependence. Figure 1.24 (right) shows the noise waveform superimposed on a small signal. As can be seen, the noise level determines the minimum signal whose presence can be discerned.

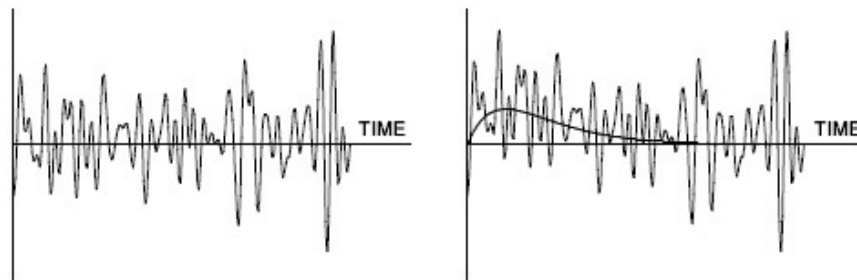
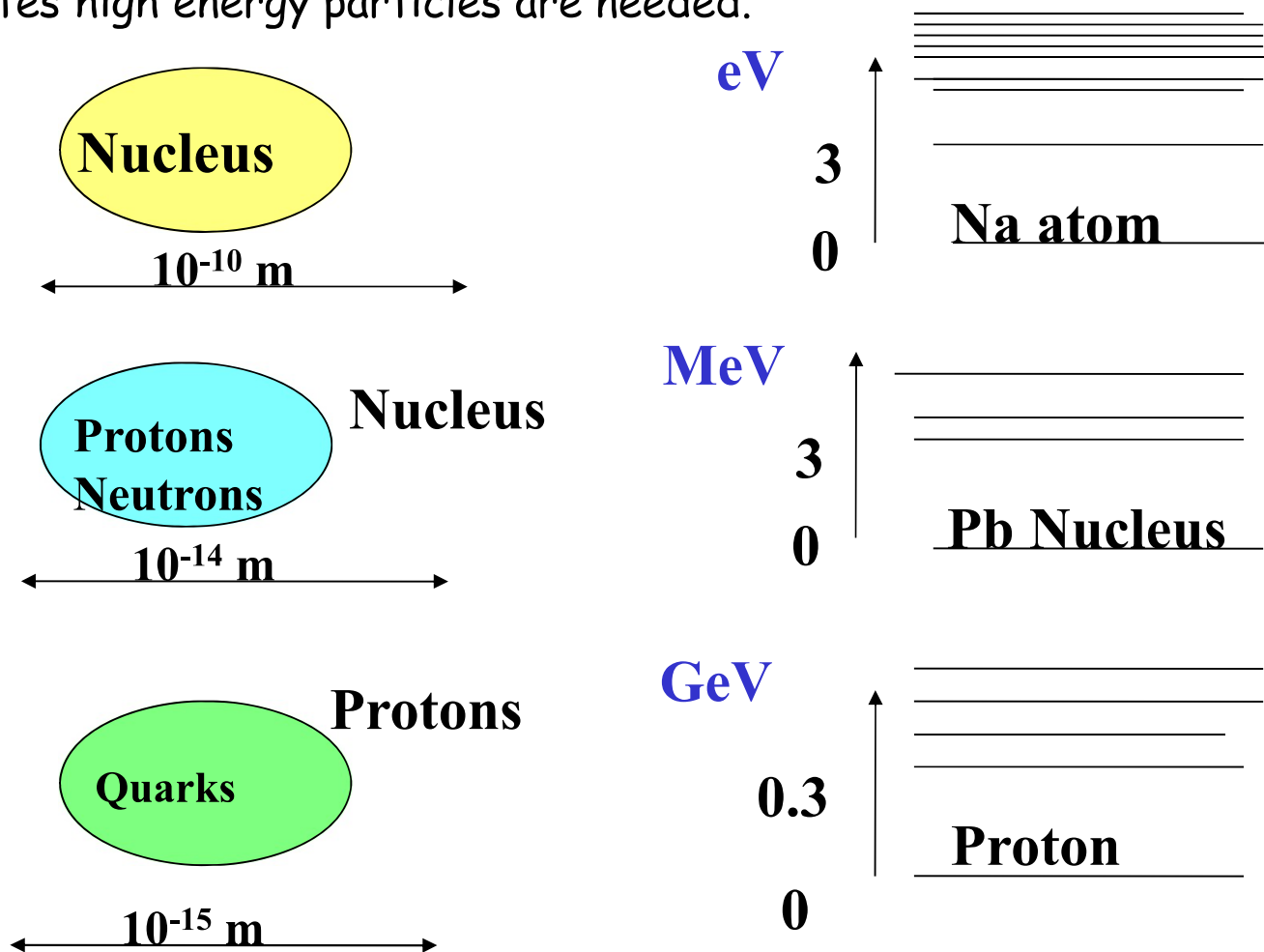


FIG. 1.24. Waveforms of random noise (left) and signal + noise (right), where the peak signal is equal to the rms noise level ($S/N = 1$). The noiseless signal is shown for comparison.

Spectroscopy:

- Experiments to determine the decay products of excited states and their interaction
- The excitation energies of a system increase as size decrease. To produce these excited states high energy particles are needed.

Absolute energies may vary a lot
But resolution usually still a critical issue



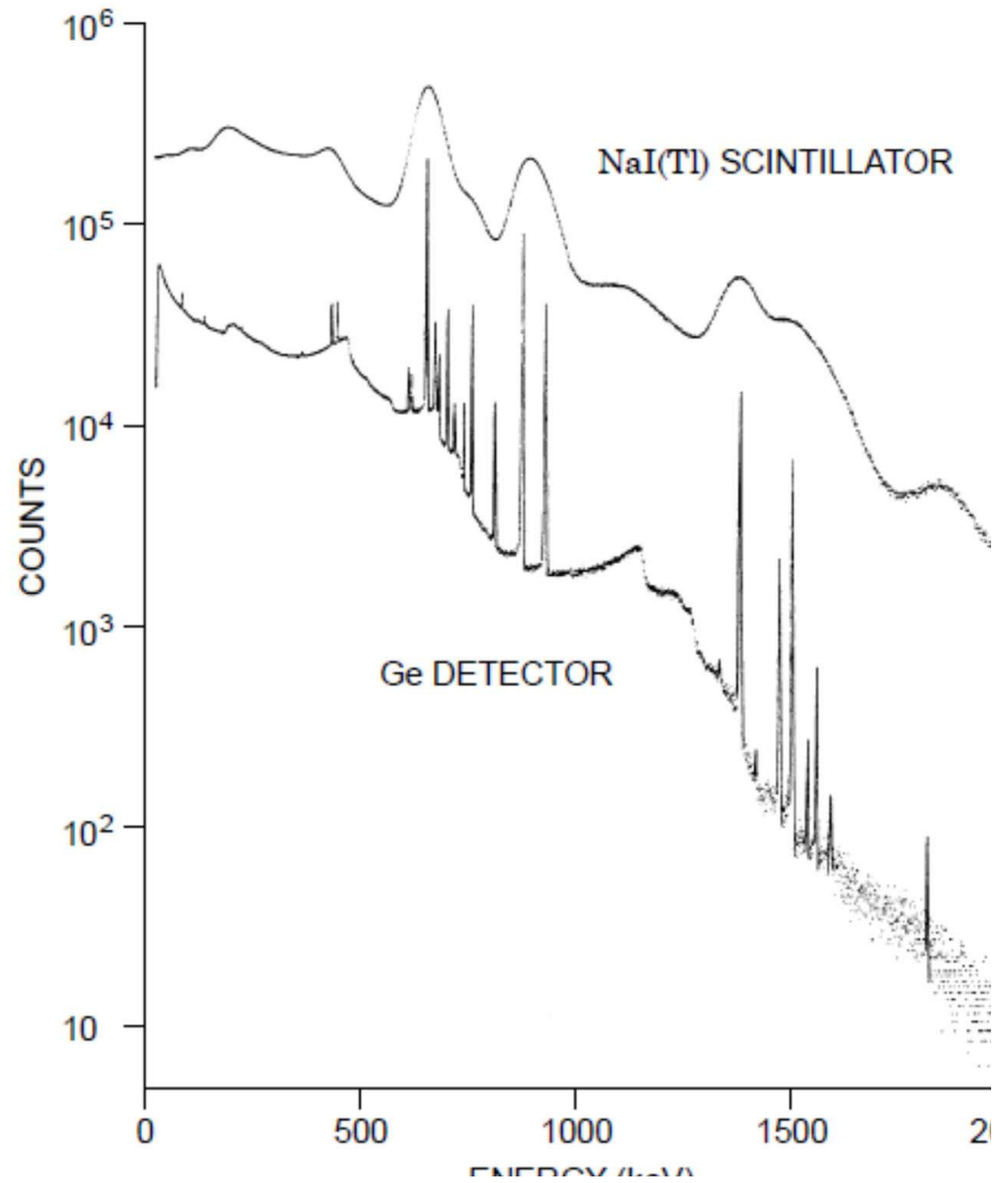
Resolution and Electronic Noise

Resolution: the ability to distinguish signal levels

Why?

Recognize structure in amplitude spectra

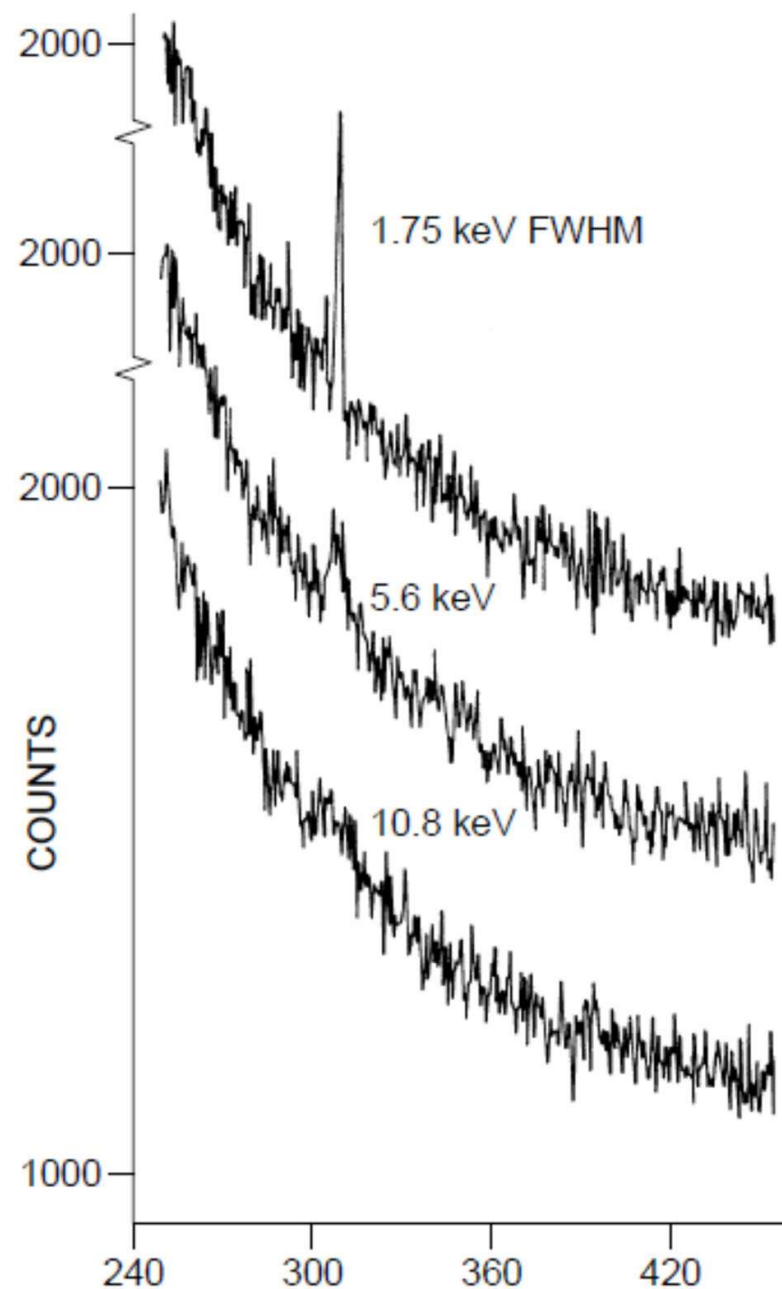
Comparison between NaI(Tl) and Ge detectors



b) Improve sensitivity

Signal to background ratio improves with better resolution

(signal counts in fewer bins compete with fewer background counts)



li di Frascati of INFN, wh
next year. The experiment,
ram, has some special f
ypernuclear physics experi
will operate at a e^+e^- collide
What follows will describe it

structure of Λ -hypernuc

Λ -hypernucleus ${}^A_\Lambda Z$ is a b
rons and a Λ hyperon. Th
ade by the $(A-1)$ nucleons:
ne nucleus $(A-1)Z$ and the
he Λ hyperon, carrying th
istinguishable baryon an
nposed by the Pauli princij
im states already filled up
hyperon, embedded in a
plore nuclear structure.

The binding energy B_Λ of
its ground state is defined

$$B_\Lambda = M$$

here M_{core} is the mass (in
e mass of the Λ particle an
 Z , experimentally measu
ope of about 1 MeV/(unit
r the heavy hypernuclei. Th
which the Λ particle is con
qual to the nuclear radius an
the 55 MeV typical value c

This is consistent with a Λ -
nucleon-nucleon one. Indec
teraction, the zero isospir

vector mesons like the π or the ρ with a nucleon and deter
ines the lack of strong tensor components in the interaction.
e relative weakness of the Λ -nucleon interaction entails that the
ell structure is not disrupted by the insertion of the Λ in the
ucleus and the lack of Pauli effects allows all the nuclear single
rticle states to be populated by the Λ . In Figure 2, the so called
egre table" of the hypernuclei shows the 35 hypernuclei known
present.

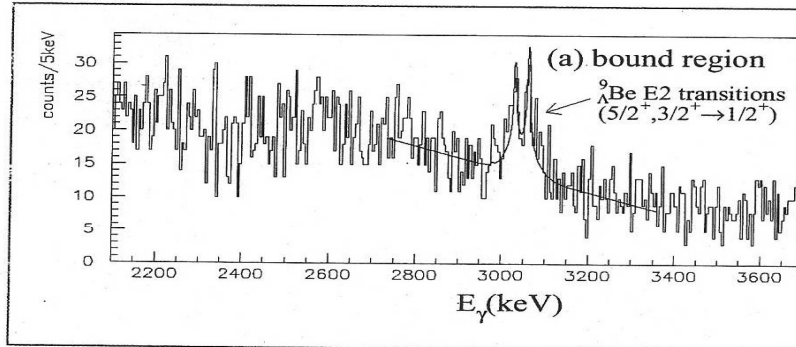
Experiments of hypernucleus production by "strangeness
change" and "associated production" processes can produce
pernuclei in which the Λ populates different single particle
tes. The latter technique is particularly suitable for populating
y lying Λ states, thanks to the high recoil momentum trans-
red to the Λ particle in the reaction.

A beautiful representation of this process is given in Figure 3,
ere the excitation spectrum of ${}^{89}_\Lambda Y$, obtained by the "associated
roduction" reaction ${}^{89}Y(\pi^+, K^+) {}^{89}_\Lambda Y$ at the KEK laboratory in
an, is shown. The spectrum demonstrates how, starting from
eutron in the $g_{9/2}$ state, it is possible to accommodate a Λ particle
the hypernuclear states f, d, p and even in the ground state s .

These measurements constitute the spectacular confirmation,
a textbook level, of the validity of the independent particle
del or shell model of the nucleus. In non-strange nuclei, the
servation of single particle states is only possible for the states
the most external nucleon orbits. In fact, due to the Pauli prin-
le and pairing interactions, deeply bound nucleon single
rticle states are so fragmented as to be essentially unobservable.
e present experimental data on hypernuclear binding energies
d detailed spectroscopic features are limited in quantity and

tion of the YN interaction.

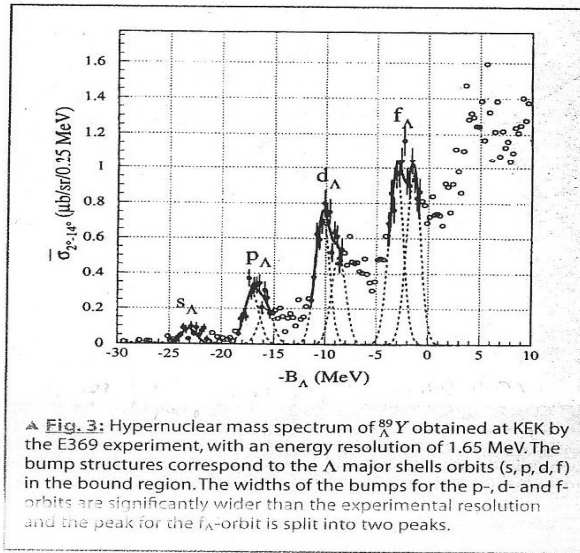
Figure 4 reports a recent measurement of the splitting of the
 $5/2^+-3/2^+$ doublet in ${}^9_\Lambda Be$ by the BNL-AGS E930 experiment [4],
measuring γ rays emitted in the nuclear transitions with the new
germanium detector array Hyperball. This new technique allowed
the energy resolution on low lying hypernuclear levels to be
improved from a few MeV to a few keV, even if the count rate
resulting is still quite low, ~ 200 γ 's per month of data taking. The
spacing of the two levels was measured to be 31 ± 2 keV, incompat-
ible with the prediction of the meson exchange models.



◀ Fig. 4
deexcit
obtaine
between
1/2+) tr
strength
The sm
31 ± 2 k
obtaine

europhysics news SEPTEMBER/OCTOBER 2002

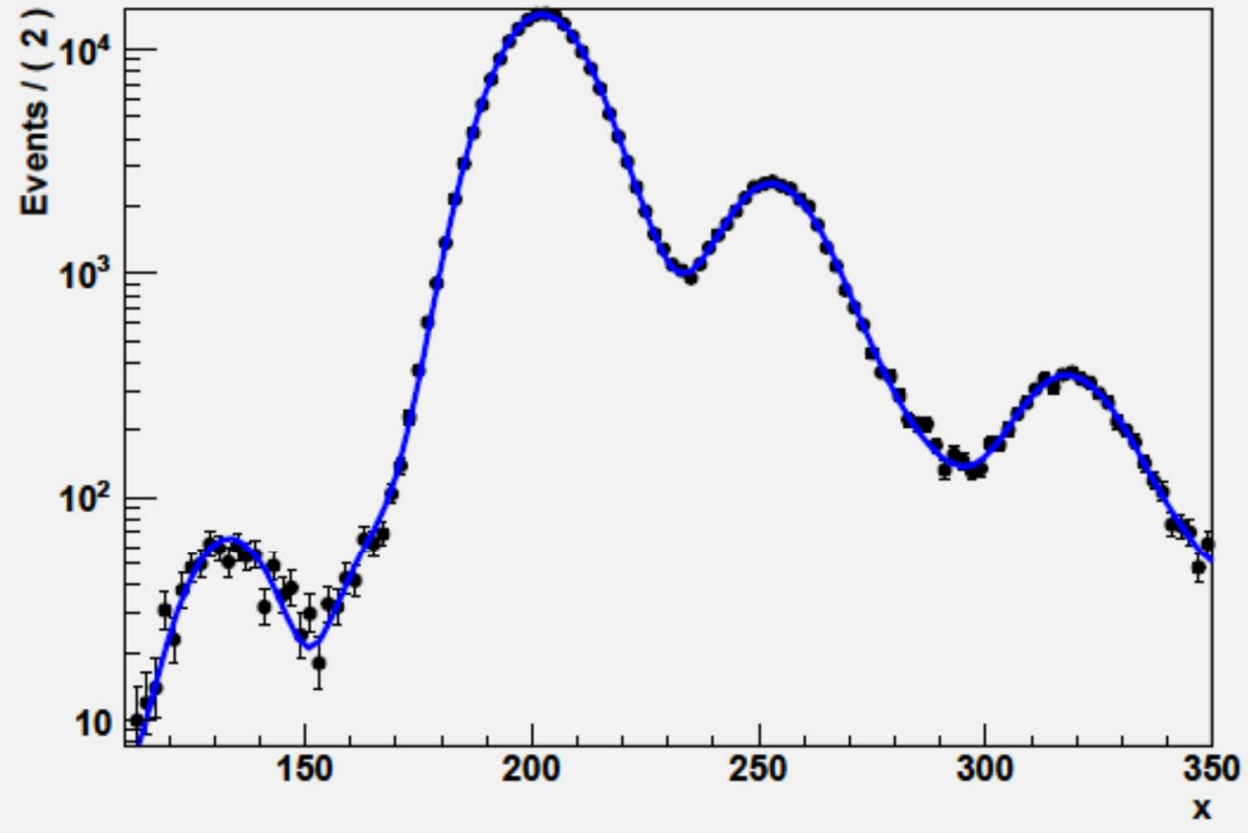
THE IMPROVEMENT OF THE YN INTERACTION MODELS WOULD NEED
precise data on the free YN interaction, which are very difficult to



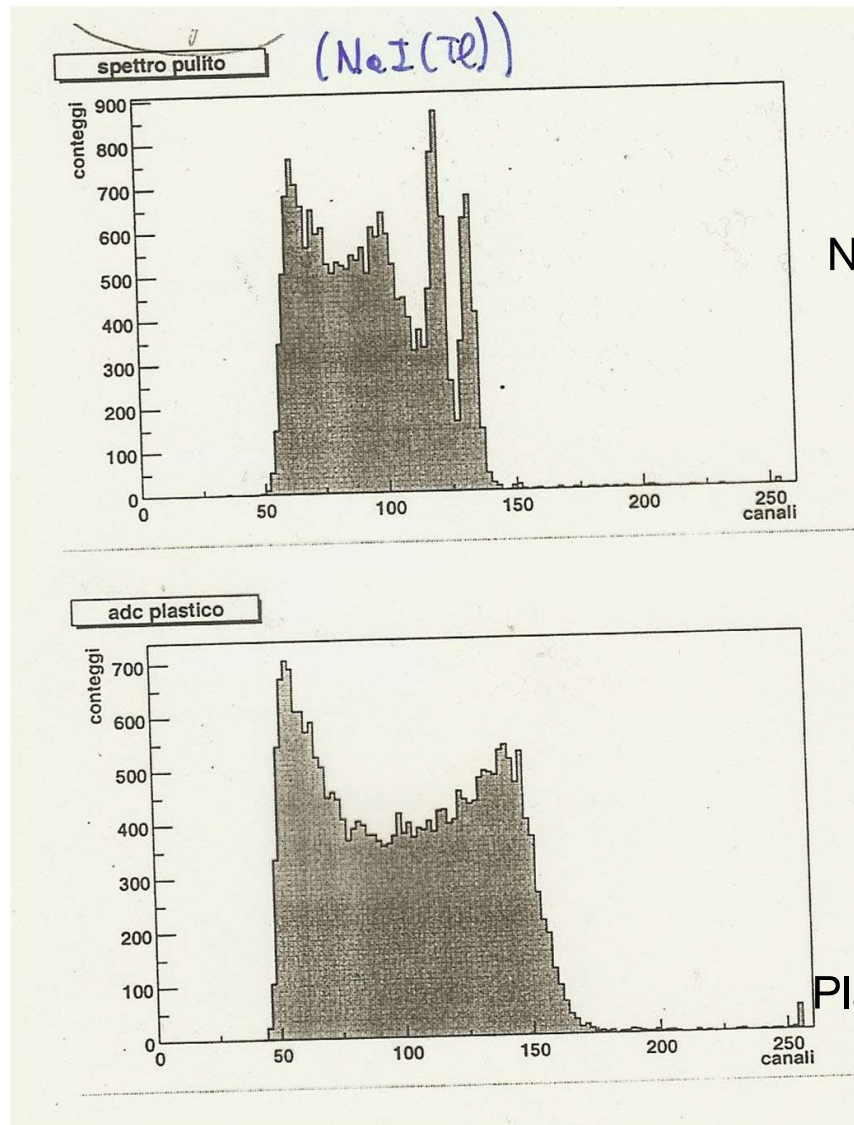
▲ Fig. 3: Hypernuclear mass spectrum of ${}^{89}_\Lambda Y$ obtained at KEK by the E369 experiment, with an energy resolution of 1.65 MeV. The bump structures correspond to the Λ major shells orbits (s, p, d, f) in the bound region. The widths of the bumps for the p -, d - and f -orbits are significantly wider than the experimental resolution and the peak for the f_Λ -orbit is split into two peaks.

europhysics news SEPTEMBER/OCTOBER 2002

A RooPlot of "x"



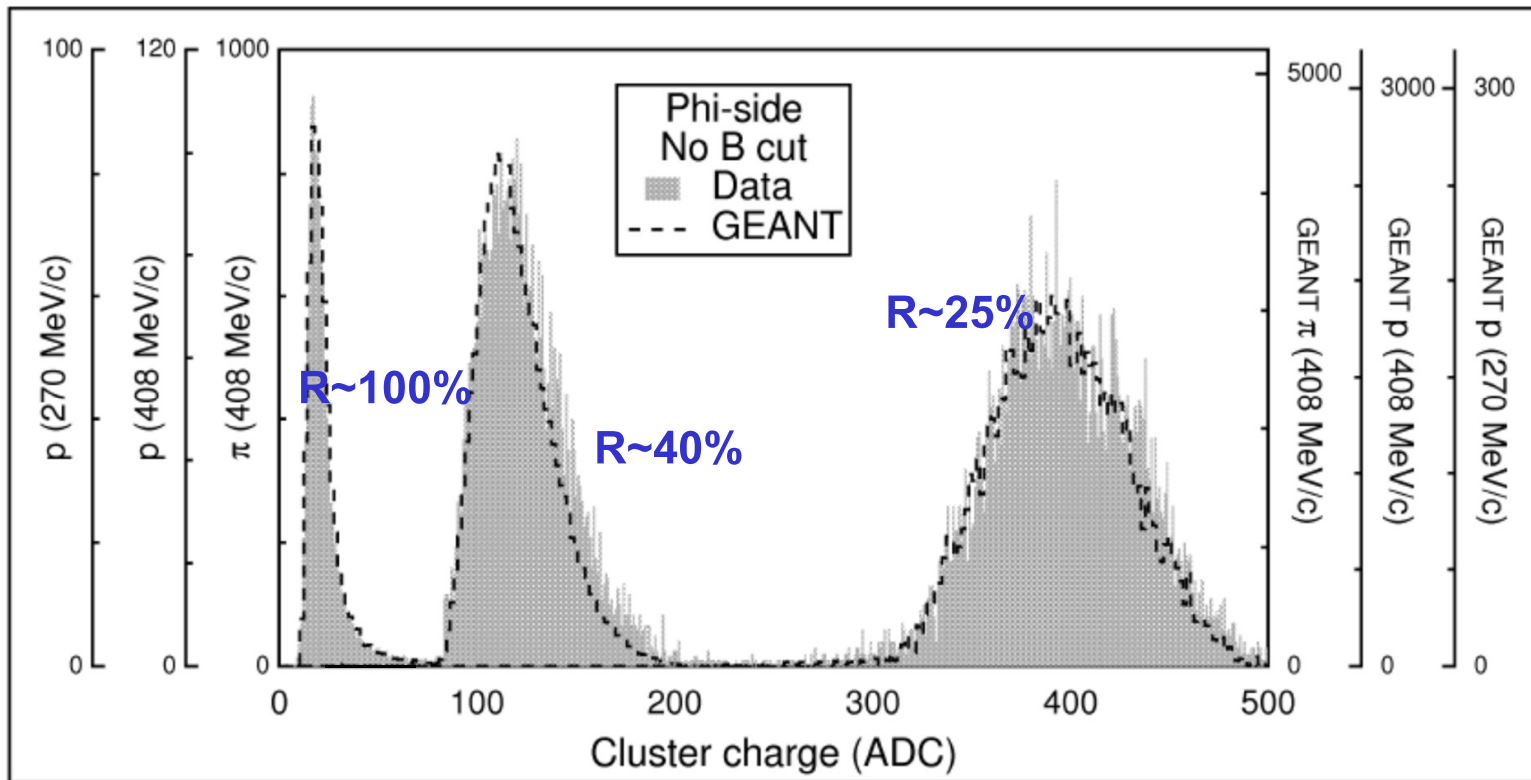
Response function

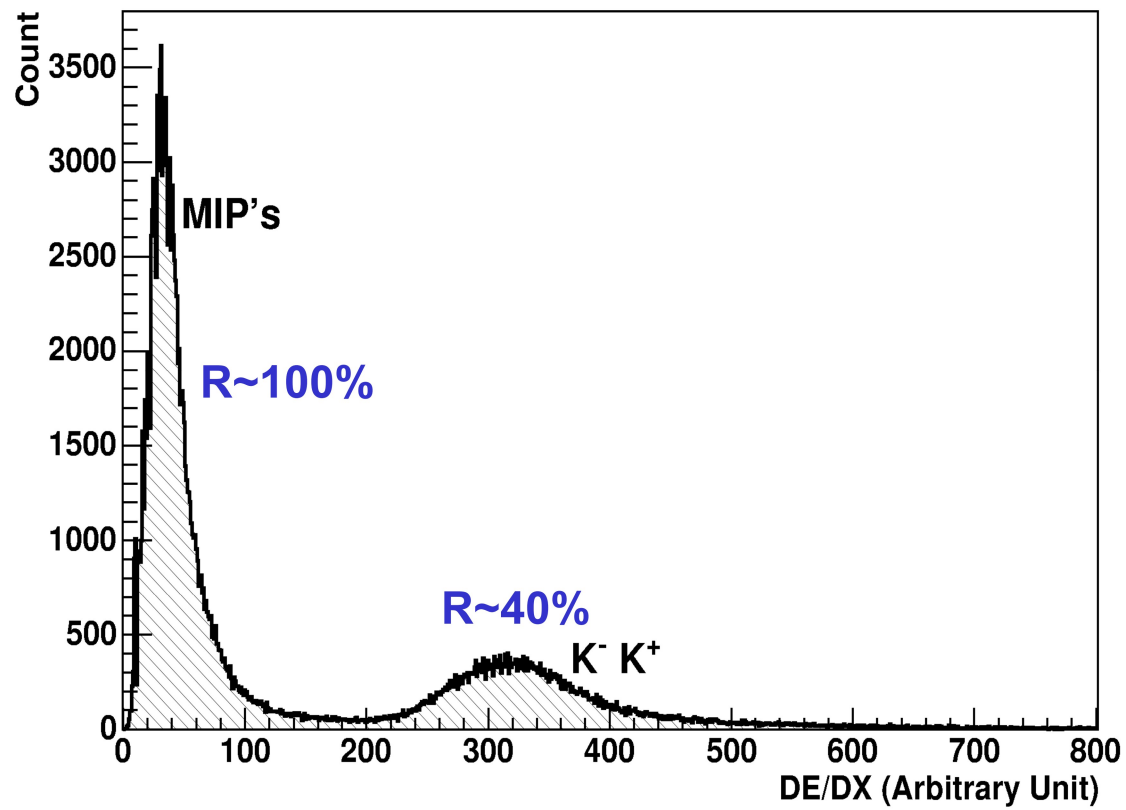


NaI(Tl) scintillator

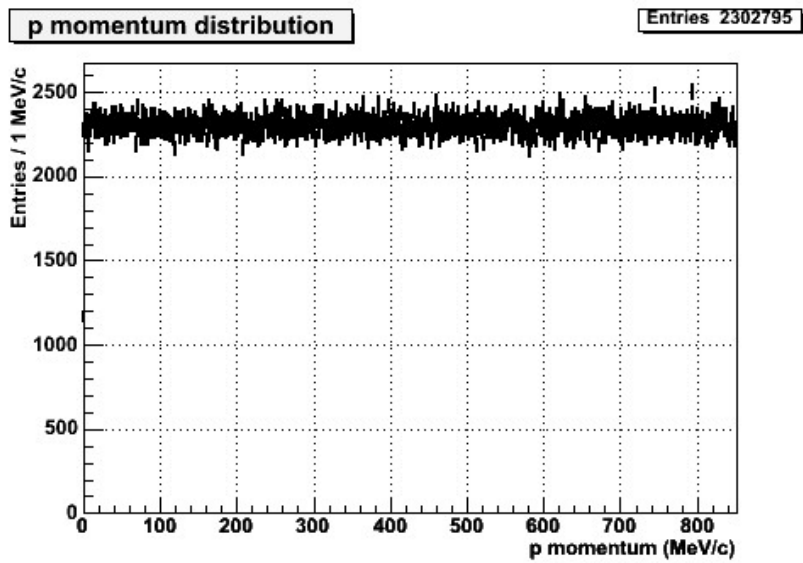
Plastic scintillator

There are actually 2
monoenergetic radiation
Sources...

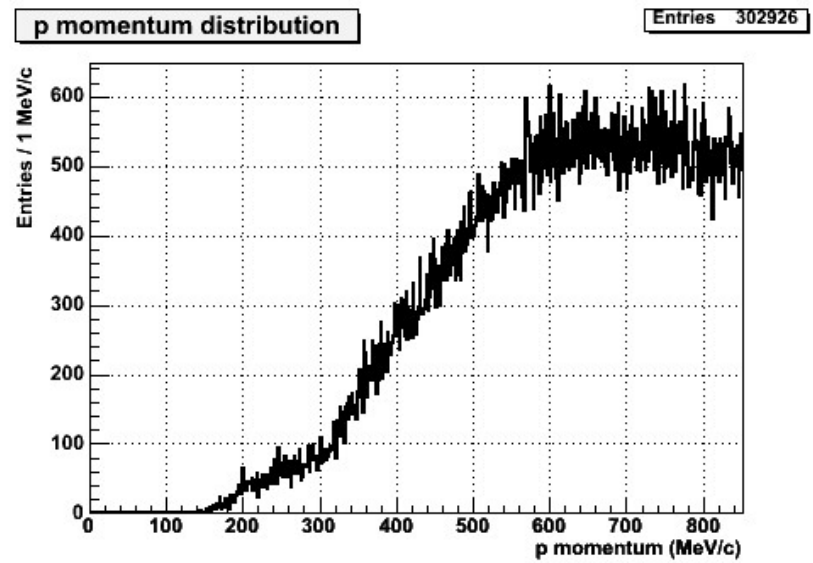




Acceptance effect on proton momentum distribution



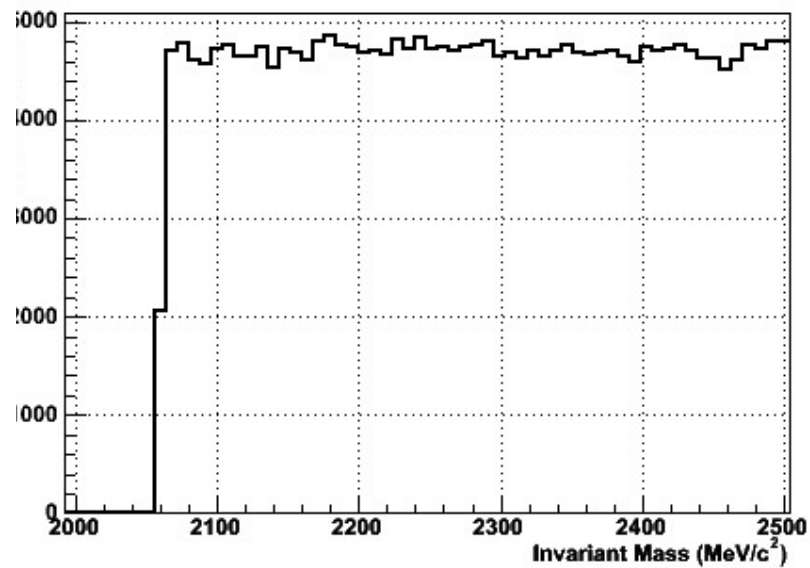
Original distribution



Reconstructed distribution

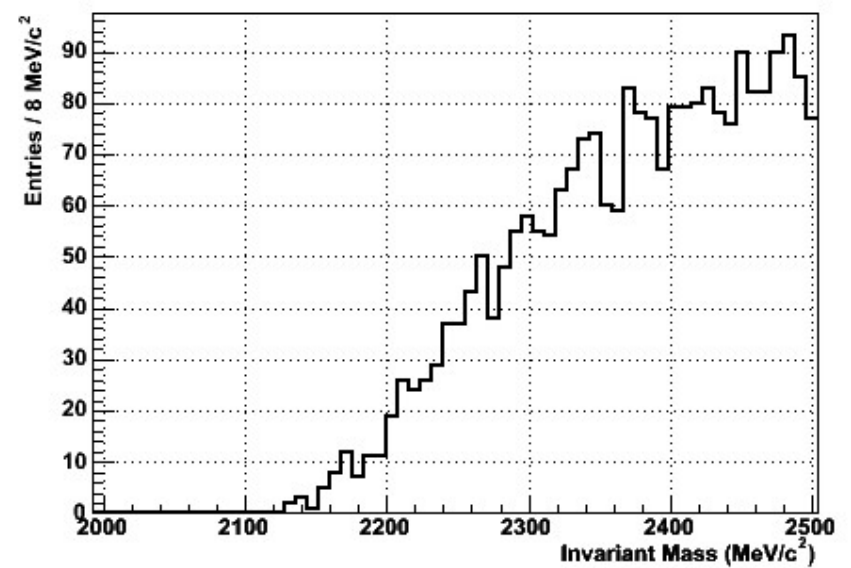
p and p invariant mass (coincidence π^+ , p, p)

Entries 588929



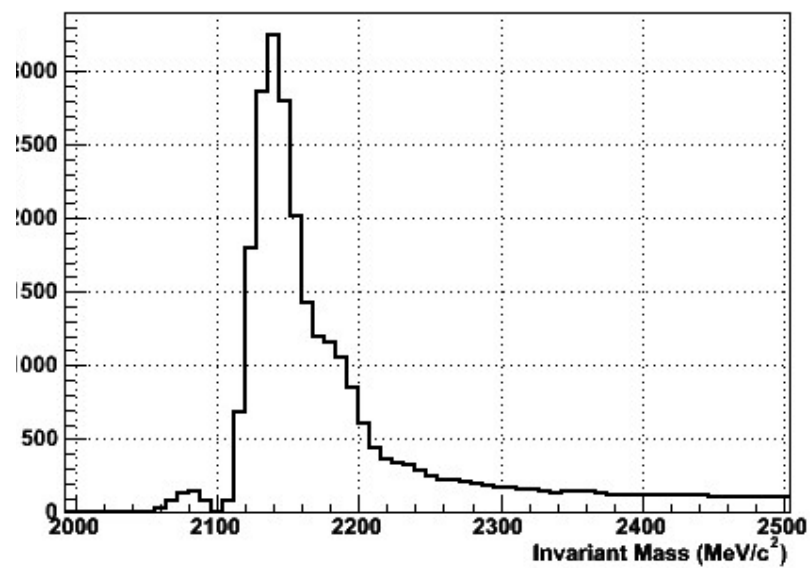
π^+ , p and p invariant mass (coincidence π^+ , p, p)

Entries 753



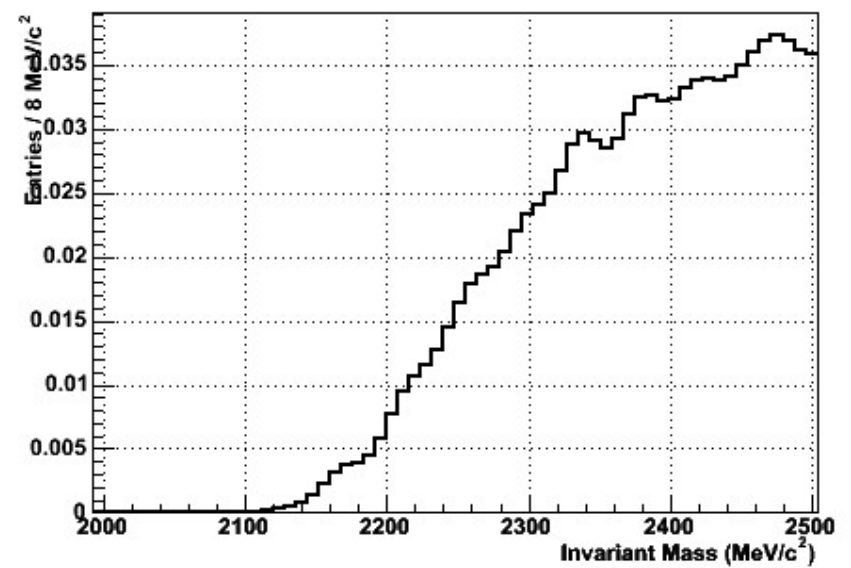
p and p invariant mass (coincidence π^+ , p, p)

Entries 589679



π^+ , p and p invariant mass (coincidence π^+ , p, p)

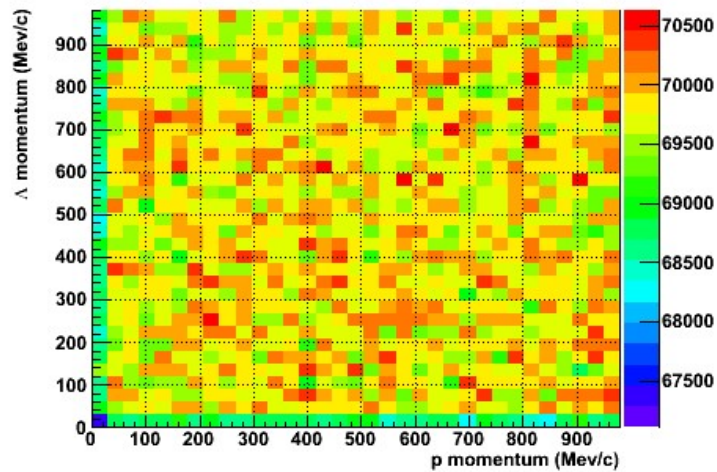
Entries 828



Λp acceptance

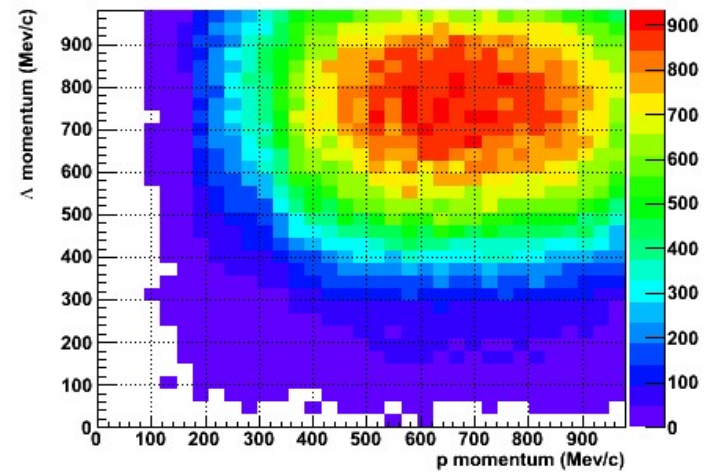
Λ momentum vs p momentum (coincidence π^- , p, p)

Entries 7.876527e+07



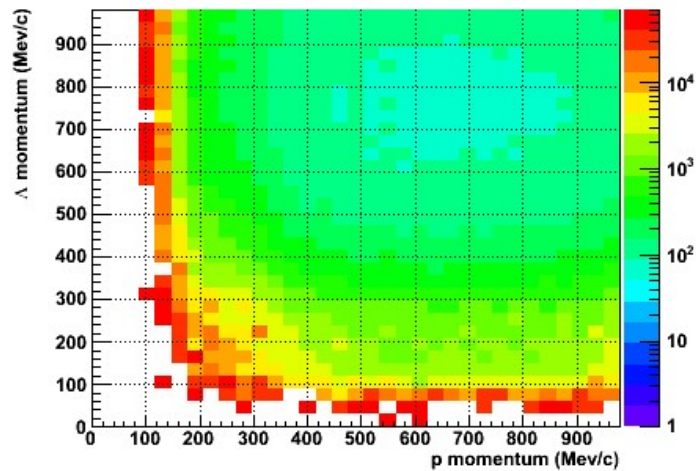
Λ momentum vs p momentum (coincidence π^- , p, p)

Entries 345297



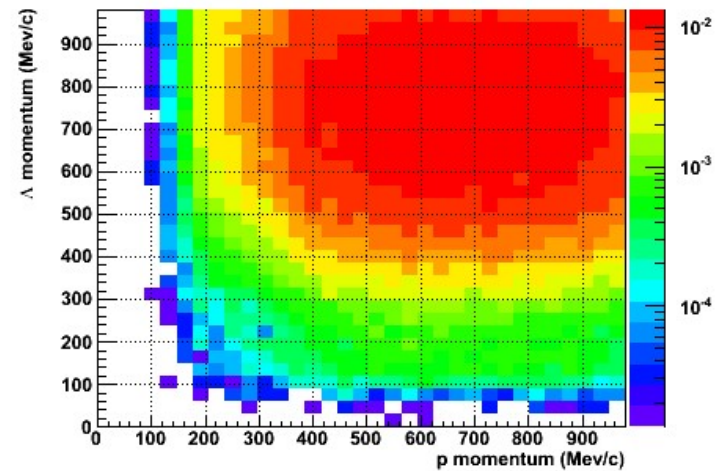
Λ momentum vs p momentum (coincidence π^- , p, p)

Entries 7.876527e+07

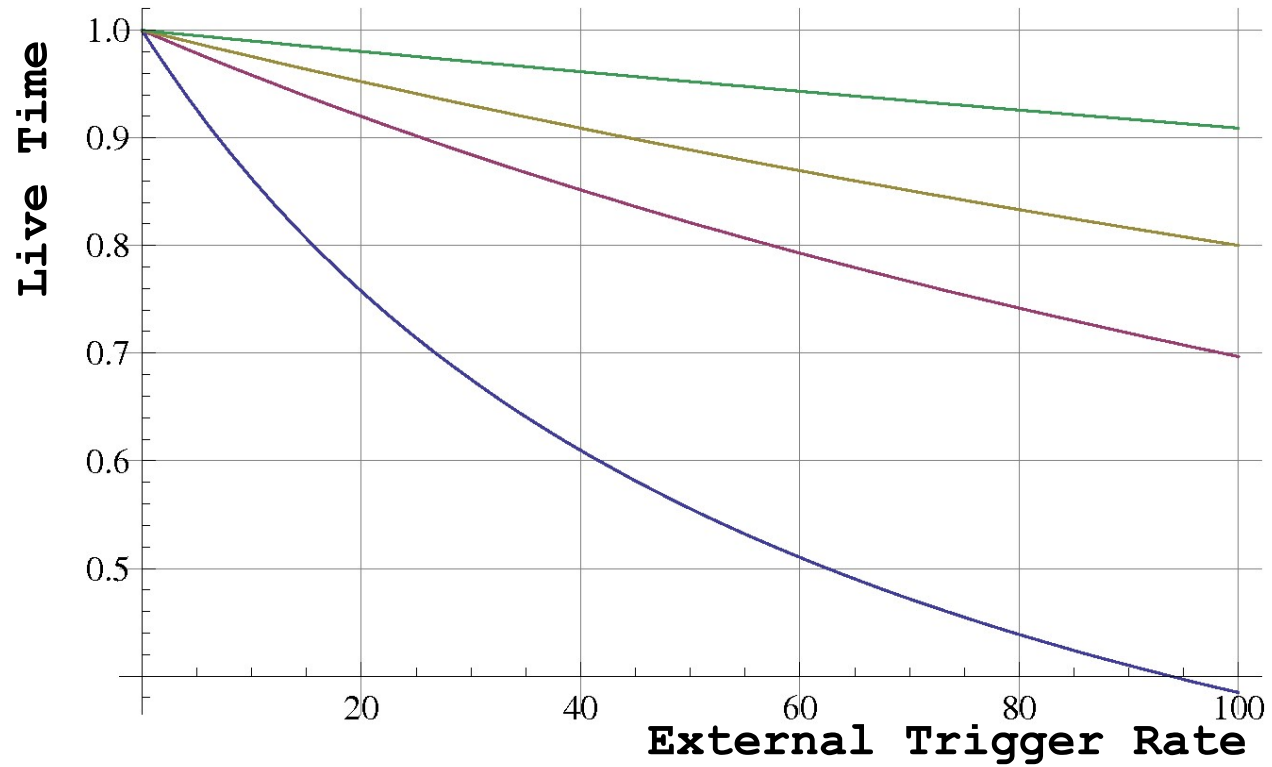


Λ momentum vs p momentum (coincidence π^- , p, p)

Entries 345297



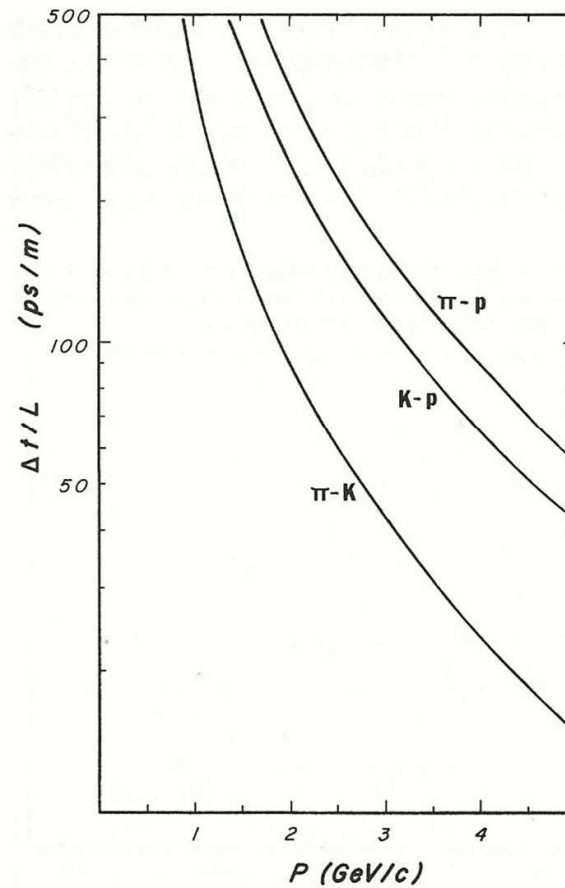
Dead time measurements



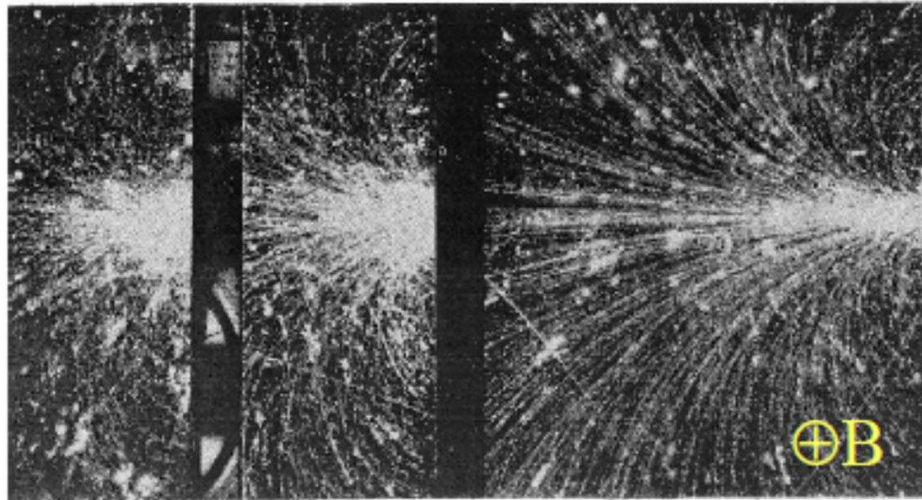
$$\text{Live time} = 1 - T_{\text{dead}}/T$$

TOF difference needed to mass discriminate particles

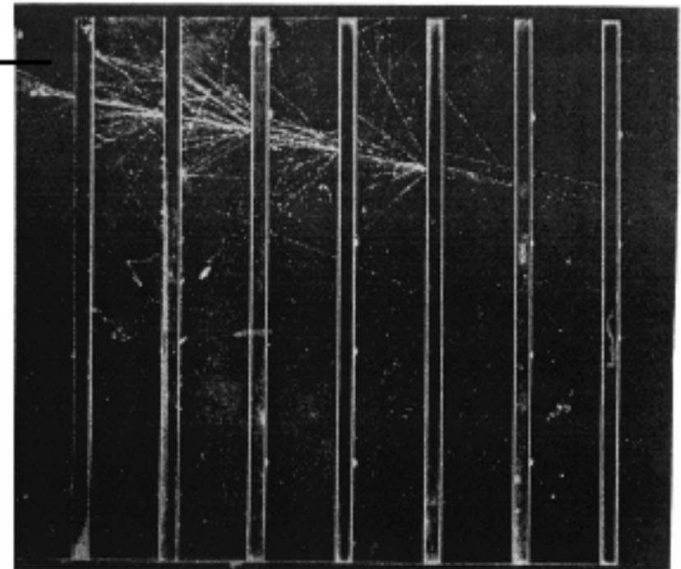
Figure 7.13 The time difference per unit flight path for π K, Kp, and π p as a function of momentum.



How a shower looks like

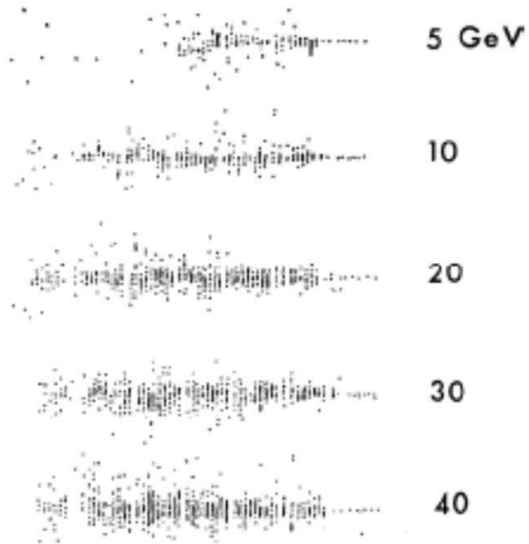


Electron shower in lead. 7500 gauss in cloud chamber. CALTECH

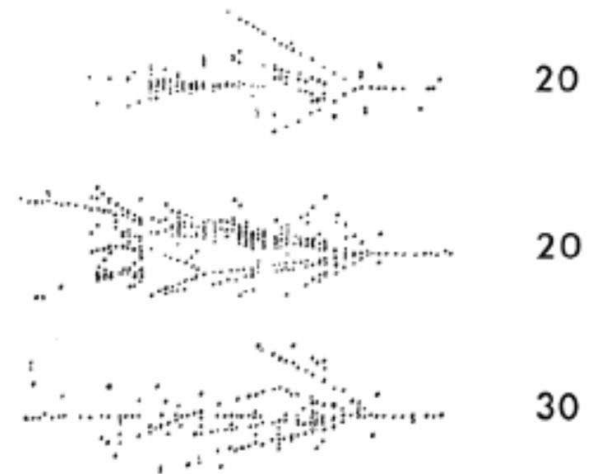


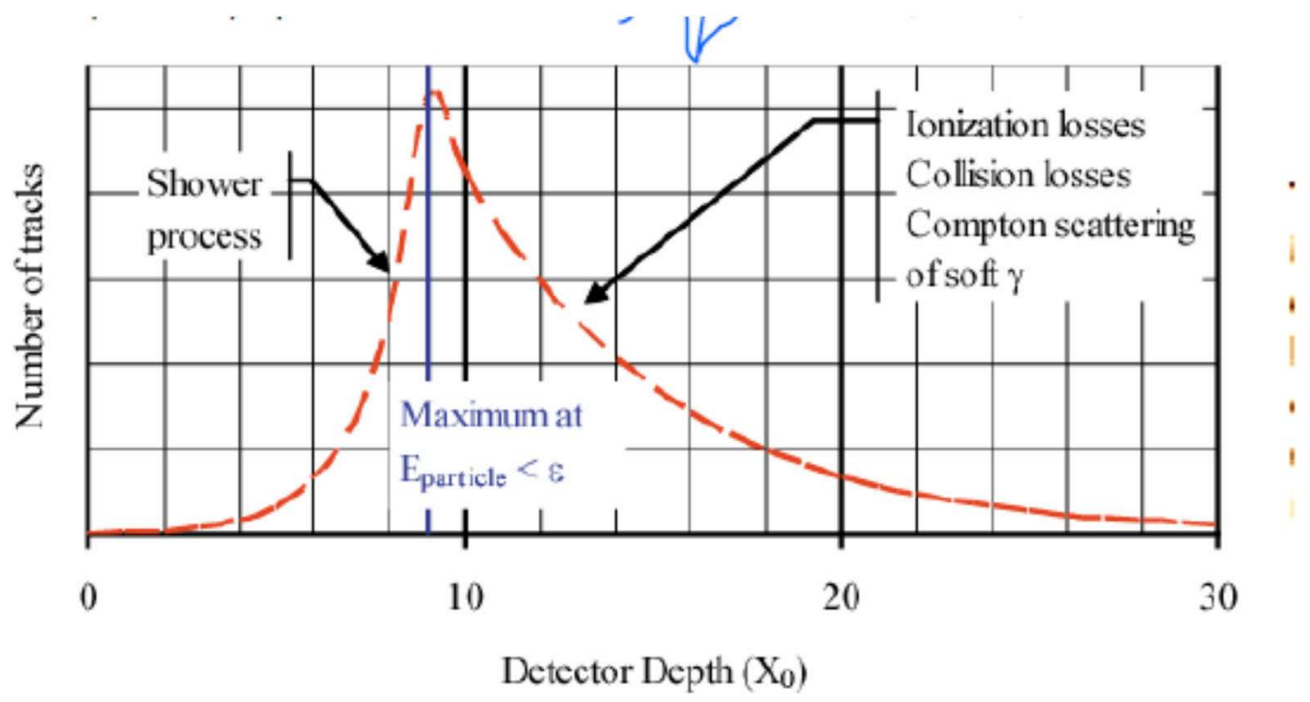
Electron shower in lead. Cloud chamber. W.B. Fretter, UCLA

Electron showers

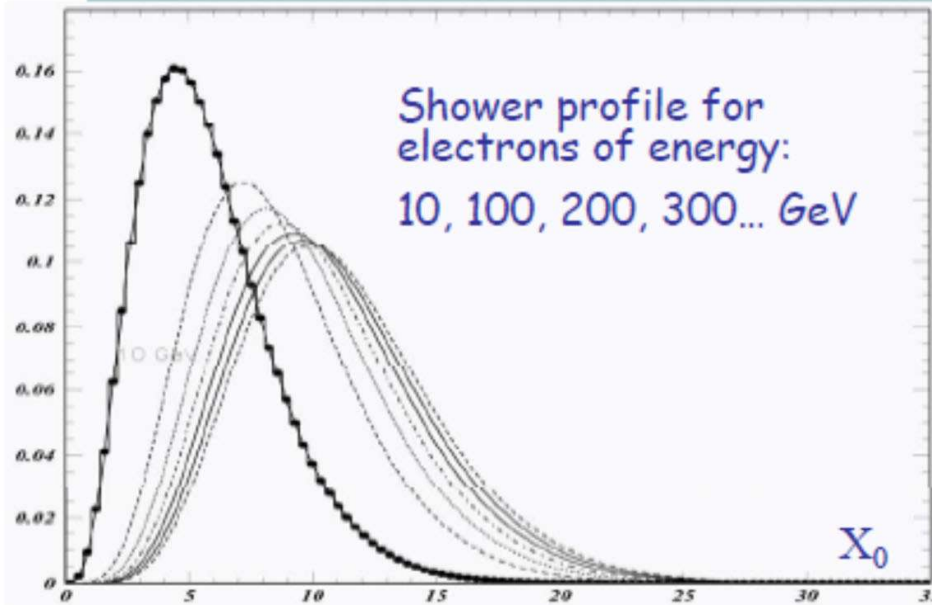


Hadron showers





EM showers: longitudinal profile



$$t_{\max} = 1.4 \ln(E_0/E_c)$$

$$N_{\text{tot}} \propto E_0/E_c$$

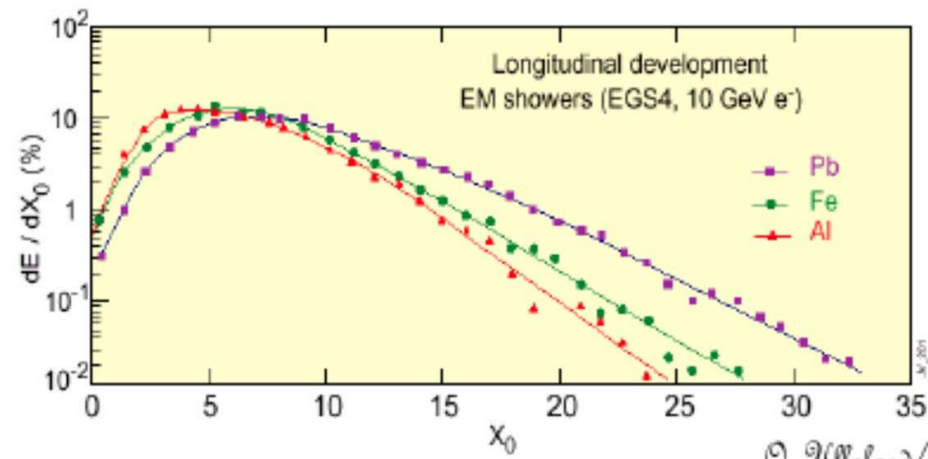
Longitudinal containment:

$$t_{95\%} = t_{\max} + 0.08Z + 9.6$$

$E_c \propto 1/Z$ \rightarrow •shower max
•shower tail

Shower parametrization

$$\frac{dE}{dt} \propto t^\alpha e^{\beta t}$$



From M. Diemoz, Torino 3-02-05

©. Ullaland/2006

EM showers: transverse profile

Transverse shower profile

- Multiple scattering make electrons move away from shower axis
- Photons with energies in the region of minimal absorption can travel far away from shower axis

Molière radius sets transverse shower size, it gives the average lateral deflection of critical energy electrons after traversing $1X_0$

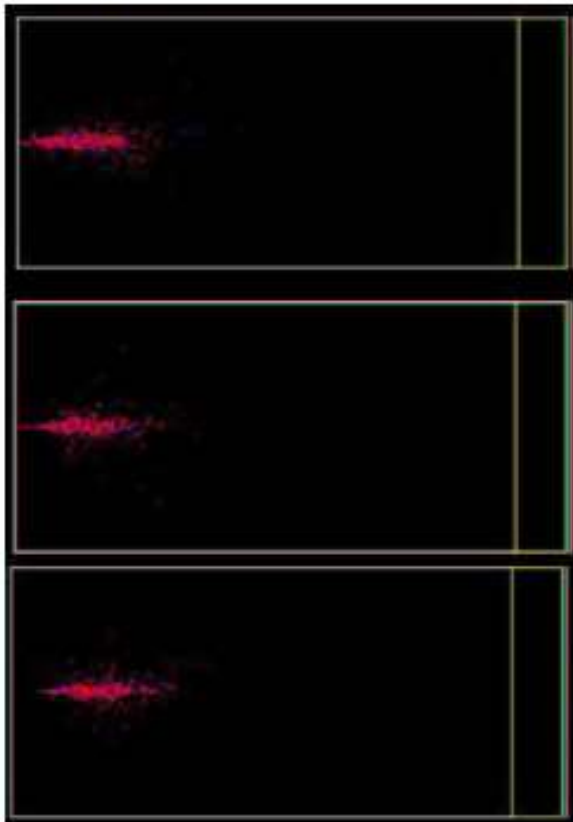
$$R_M = \frac{21\text{MeV}}{E_C} X_0$$

$$R_M \propto \frac{X_0}{E_C} \propto \frac{A}{Z} (Z \gg 1)$$

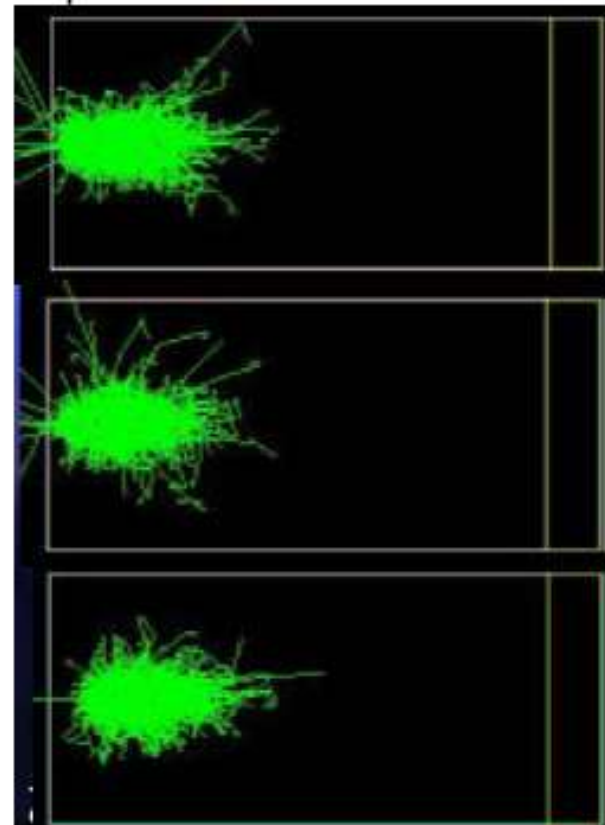
75% E_0 within $1R_M$, 95% within $2R_M$, 99% within $3.5R_M$

20 GeV γ in copper (simulation)

charged particles only



all particles



Electromagnetic calorimeters.

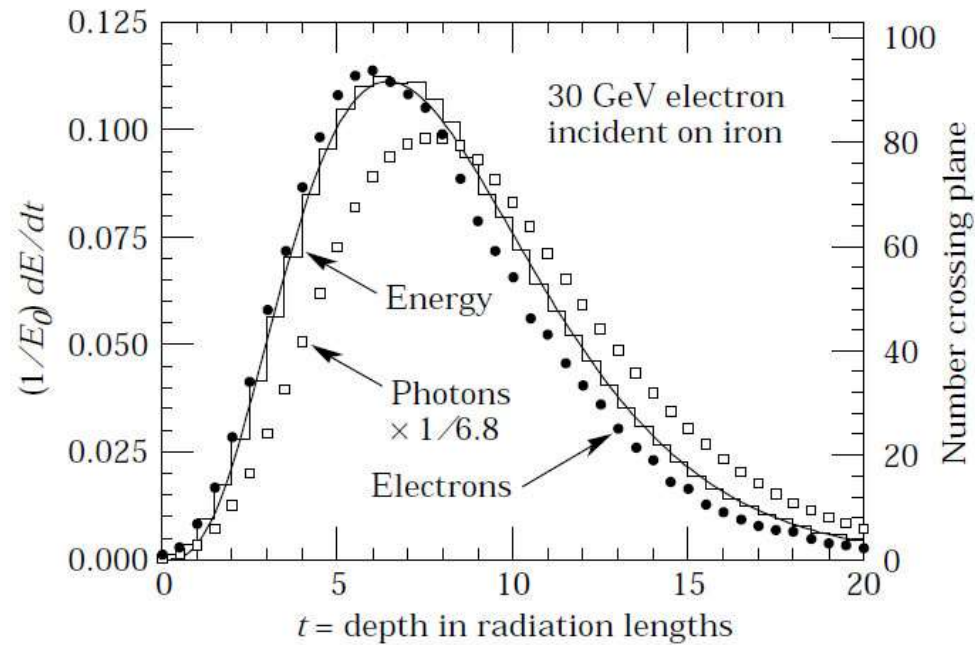


Figure 27.18: An EGS4 simulation of a 30 GeV electron-induced cascade in iron. The histogram shows fractional energy deposition per radiation length, and the curve is a gamma-function fit to the distribution. Circles indicate the number of electrons with total energy greater than 1.5 MeV crossing planes at $X_0/2$ intervals (scale on right) and the squares the number of photons with $E \geq 1.5$ MeV crossing the planes (scaled down to have same area as the electron distribution).

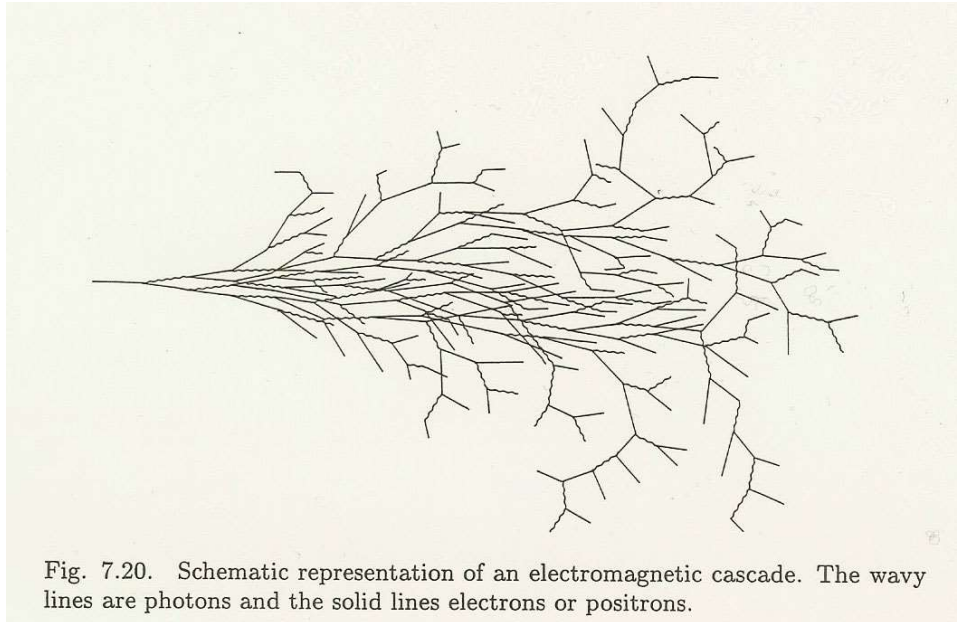


Fig. 7.20. Schematic representation of an electromagnetic cascade. The wavy lines are photons and the solid lines electrons or positrons.

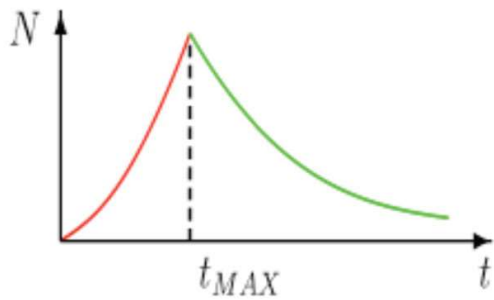


Figure 11.2 Shower profiles in lead. The number of electrons should be multiplied by a normalization factor of 0.79. (D. Müller, Phys. Rev. D 5: 2677, 1972.)

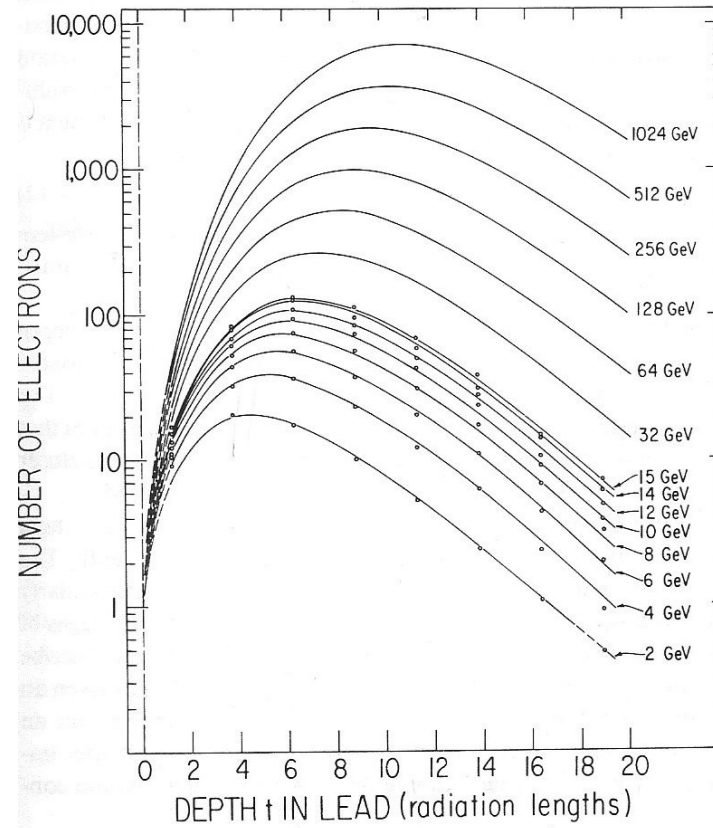
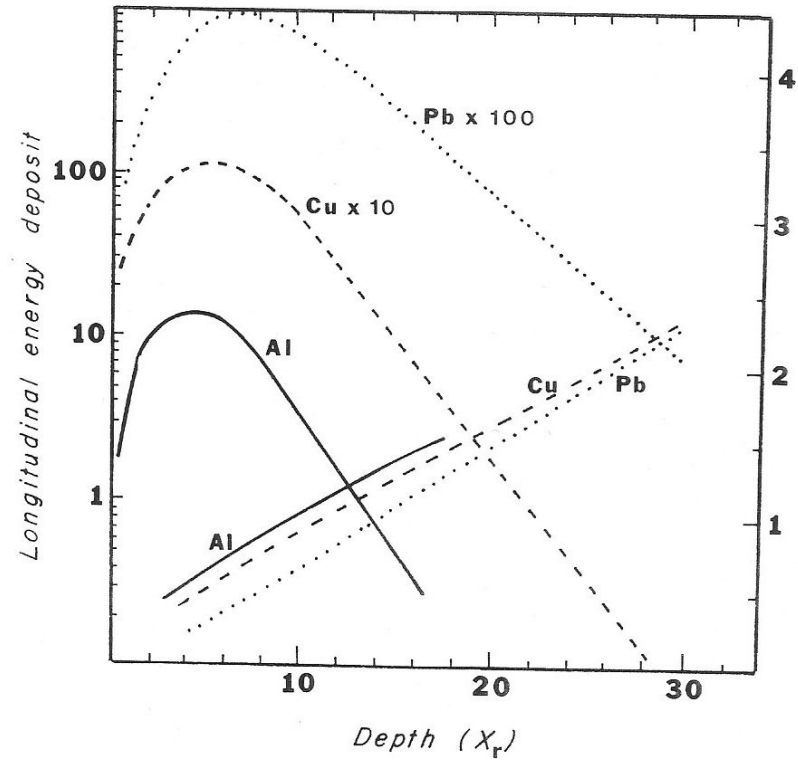


Figure 11.3 Longitudinal development of electromagnetic showers different materials. Right scale shows radii for 90% shower container (C. Fabjan and T. Ludlam, adapted with permission from the Annual Review of Nuclear and Particle Science, Vol. 32, © 1982 by Annual Reviews, Inc.)



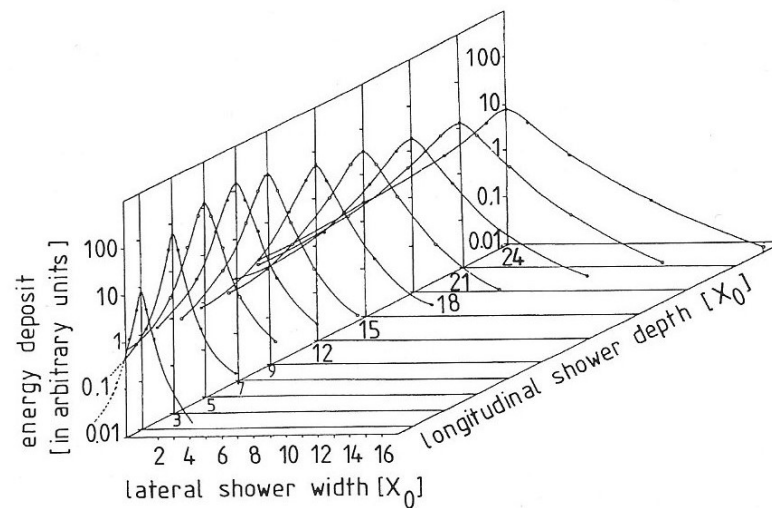
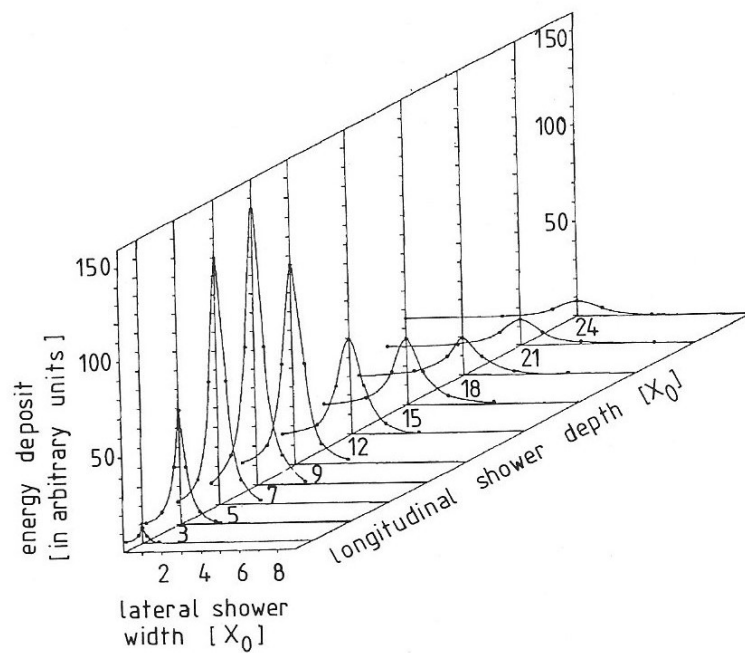
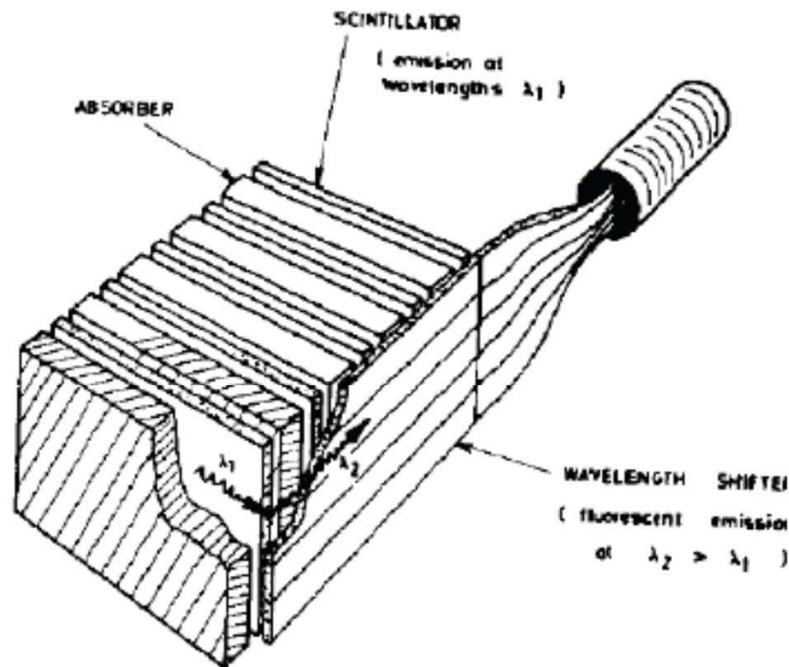


Fig. 7.23. Longitudinal and lateral development of an electron shower (6 GeV) in lead shown with linear and logarithmic scales (based on [504, 505]).



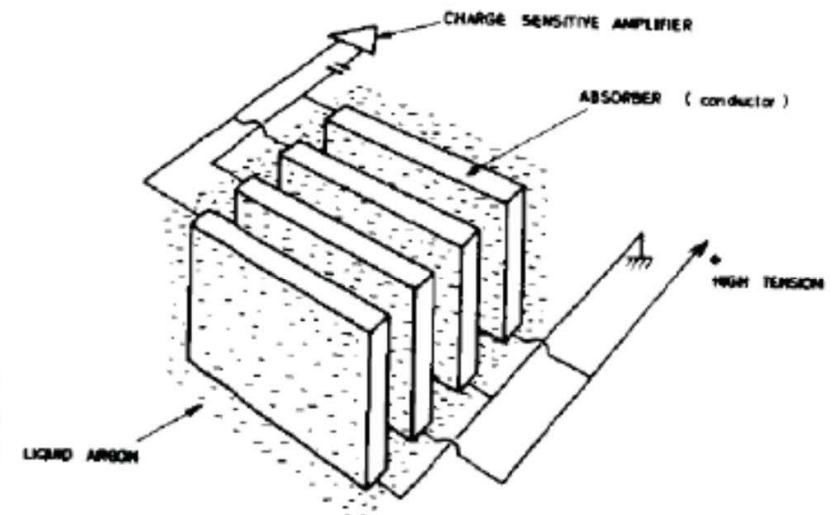
■ Basic readout types for sampling calorimeters

□ Metal-scintillator sandwich structure



C. Fabjan and T. Ludlam, 1987

□ Metal-liquid argon ionization chamber

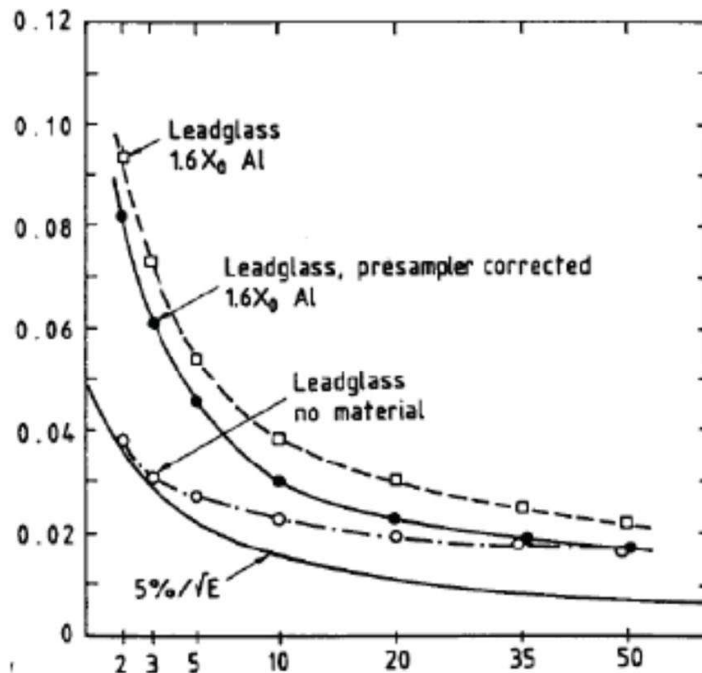


C. Fabjan and T. Ludlam, 1987

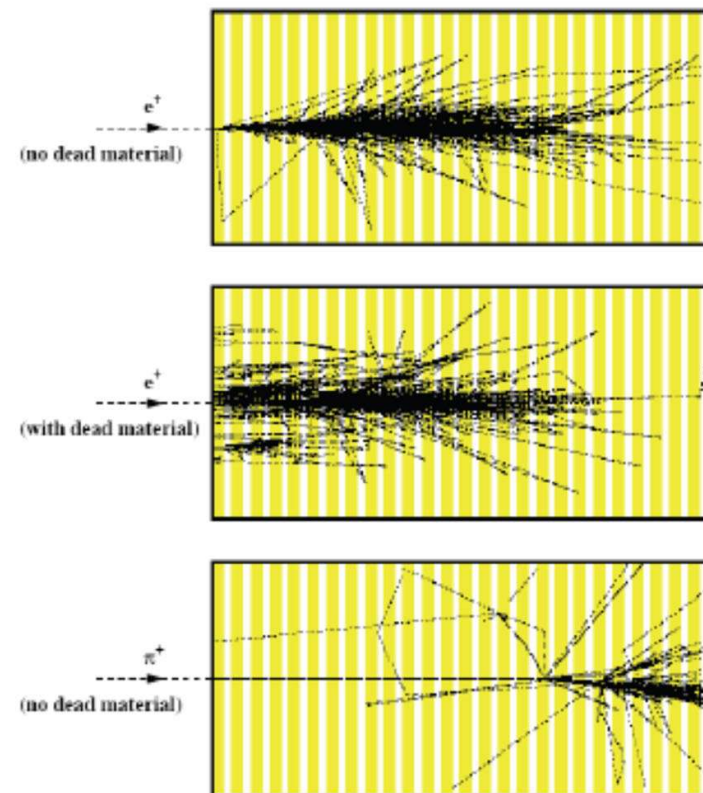


■ Energy resolution: Limitations

□ Dead material effects



OPAL collaboration, C. Beard et al. NIM A 286 (1990) 117.



Shower simulation

EM calorimeters used for mass discrimination

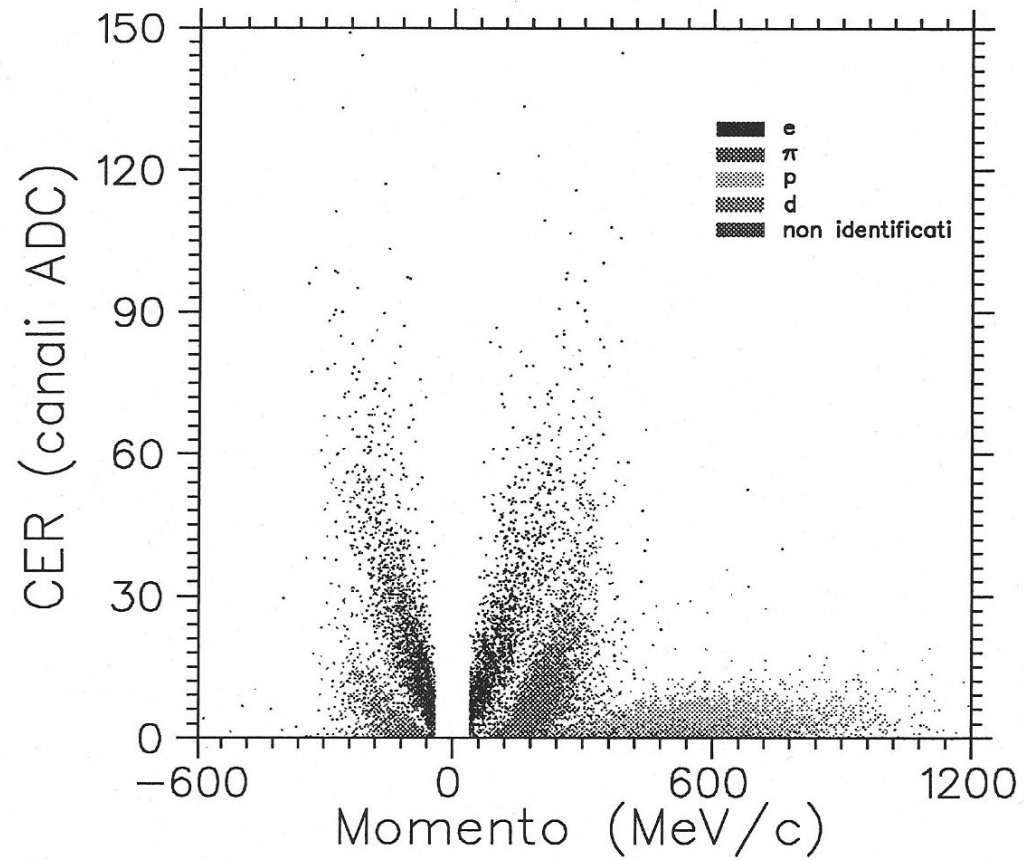


Figura 6.16: Distribuzione dei punti rappresentativi sullo scatterplot (*CER vs momento*), delle particelle cariche rivelate dallo spettrometro CHAOS, ottenuta dopo la procedura di identificazione. Nel grafico sono mostrate le particelle con tutti i gradi di identificazione (PID).

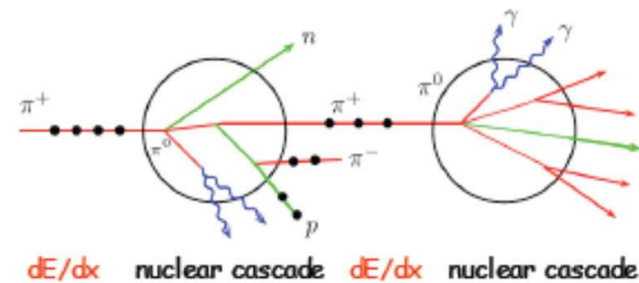


Hadronic showers

■ Hadronic shower development

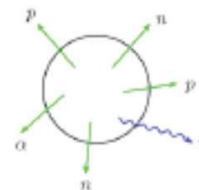
- General comment: Complexity of hadronic and nuclear processes produce multitude of effects that determine the functioning and performance of hadron calorimeters
 - Many channels compete in the development of hadronic showers
 - Larger variations in the deposited and visible energy
 - More complicated to optimize
- Sizeable electromagnetic (e) besides hadronic (h) shower contribution mainly from π^0 decay (1/3 of pions)
- Invisible energy due to delayed emitted photons in nuclear reactions, soft neutrons and binding energy
- Visible energy smaller for hadronic (h) than for electromagnetic (e) showers: Ratio of response $e/h > 1$
- Larger intrinsic fluctuations for hadronic than electromagnetic showers
- Improvements: Increase visible energy to get $e/h=1$: Compensation (Compensation for the loss of invisible energy)
- Discussed instr. effects for e showers also hold for h showers

Step 1: Production of energetic hadrons with a mean free path given by the nuclear interaction lengths

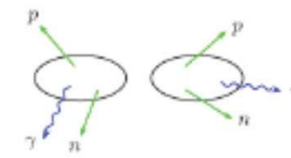


Step 2: Hadronic collisions with material nuclei (significant part of the primary part of primary energy is consumed in nuclear processes):

Evaporation



Evaporation followed by evaporation



Processes contributing to the energy deposition in hadronic cal.

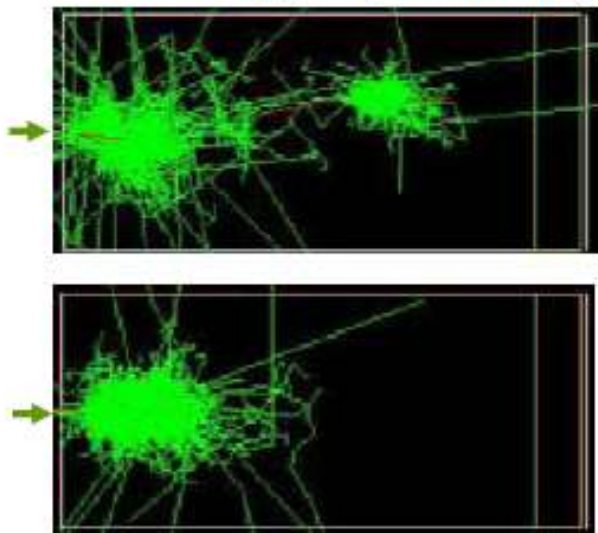
Table 11.2. *Average fractional energy deposition for a 10-GeV proton in an iron/liquid argon calorimeter*

Process	Percent of total
Secondary proton ionization	31.6
Electromagnetic cascade (π^0)	21.0
Nuclear binding energy plus neutrino energy	20.6
Secondary π^\pm ionization	8.2
Neutrons with $E > 10$ MeV	4.9
Neutrons with $E < 10$ MeV	3.9
Residual nuclear excitation energy	3.7
$Z > 1$ ionization	2.4
Primary proton ionization	2.3
Other	1.4

Source: T. Gabriel and W. Schmidt, Oak Ridge National Laboratory report, ORNL/TM-5105, 1975.

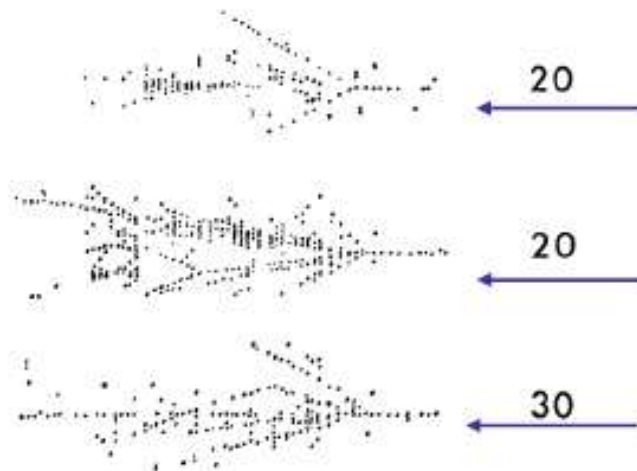
Hadronic Calorimeters (are [very] difficult to model)

20 GeV π in copper (simulation)



J.P. Wellisch

Hadron showers



Hadronic Showers (π, n, p, \dots)

Propagation : inelastic hadron interactions
→ multi particle production
Nuclear disintegration

Neutrino

Weak interactions
secondaries : mostly hadrons

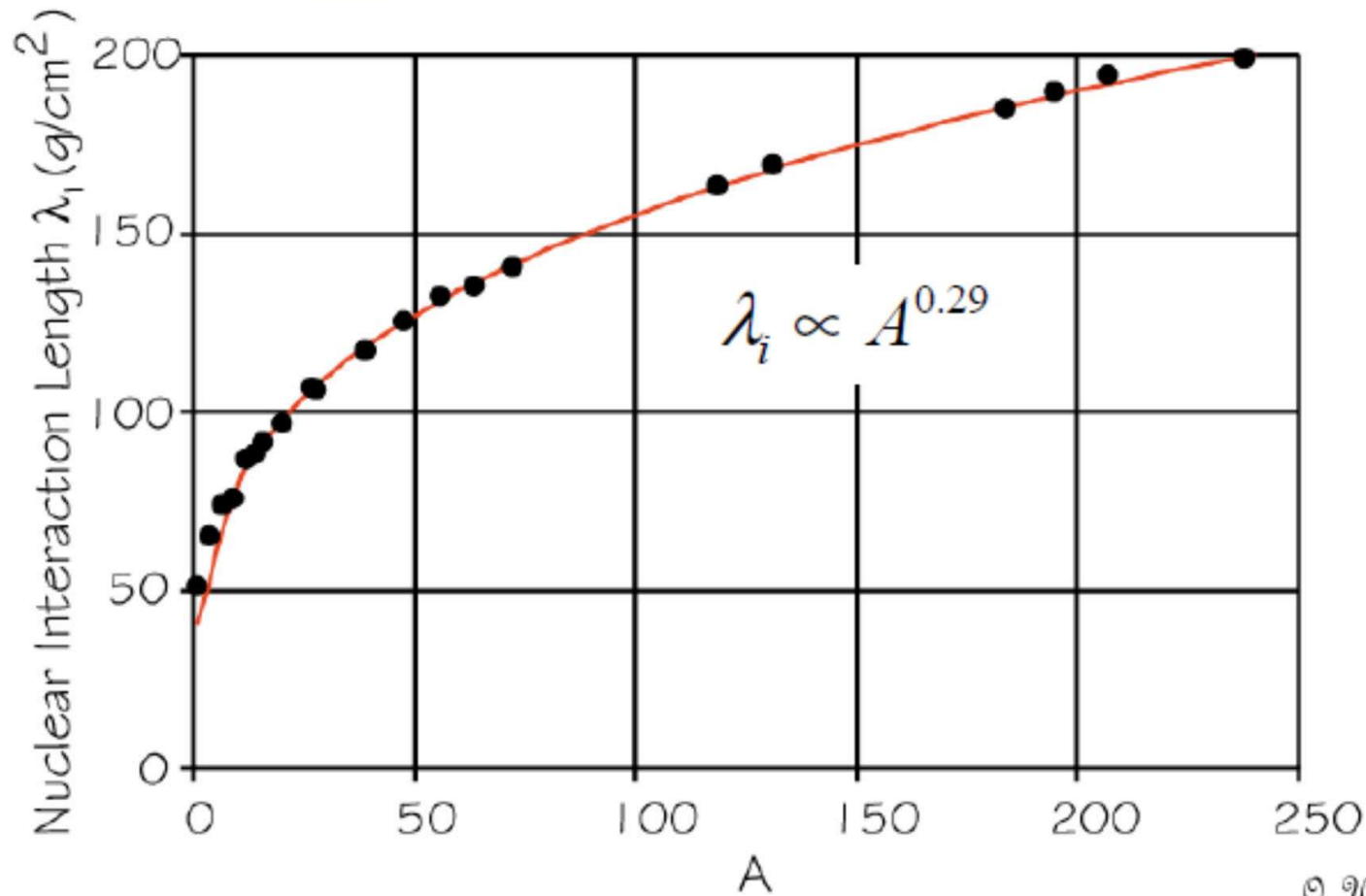
very **LARGE**



Nuclear Interaction Length λ_i

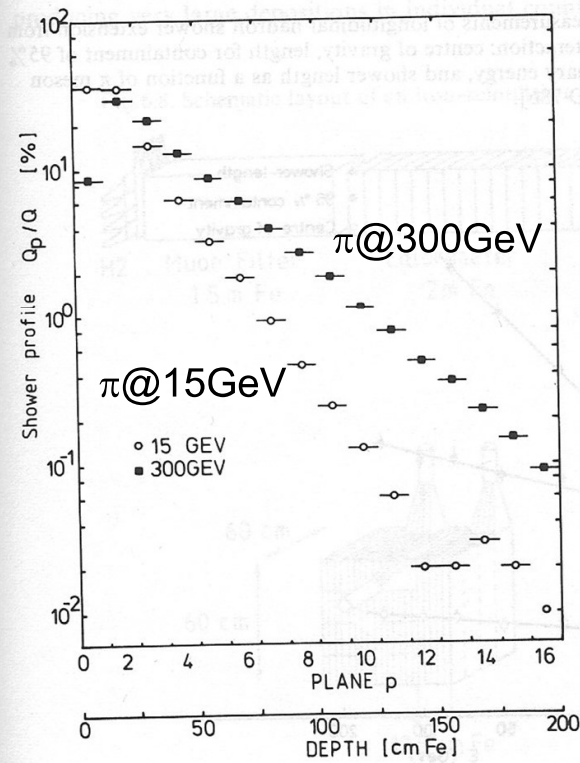
is the average distance a high-energy hadron has to travel inside a medium before a nuclear interaction occurs.

Probability not to have interacted after a path z $P = e^{-z/\lambda_i}$



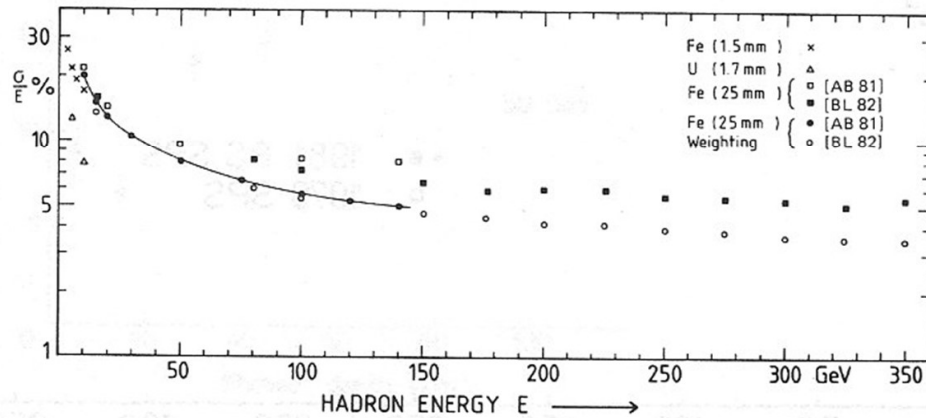
Longitudinal distribution of energy in hadron calorimeter.

Fig. 6.6. Longitudinal distribution of energy deposited in a hadron calorimeter; Q_p is the energy deposited in counter p consisting of five layers with 2.5 cm iron and 0.5 cm scintillator each; $Q = \sum Q_p$. Measurements for π mesons of 15 GeV and 300 GeV [BL 82].

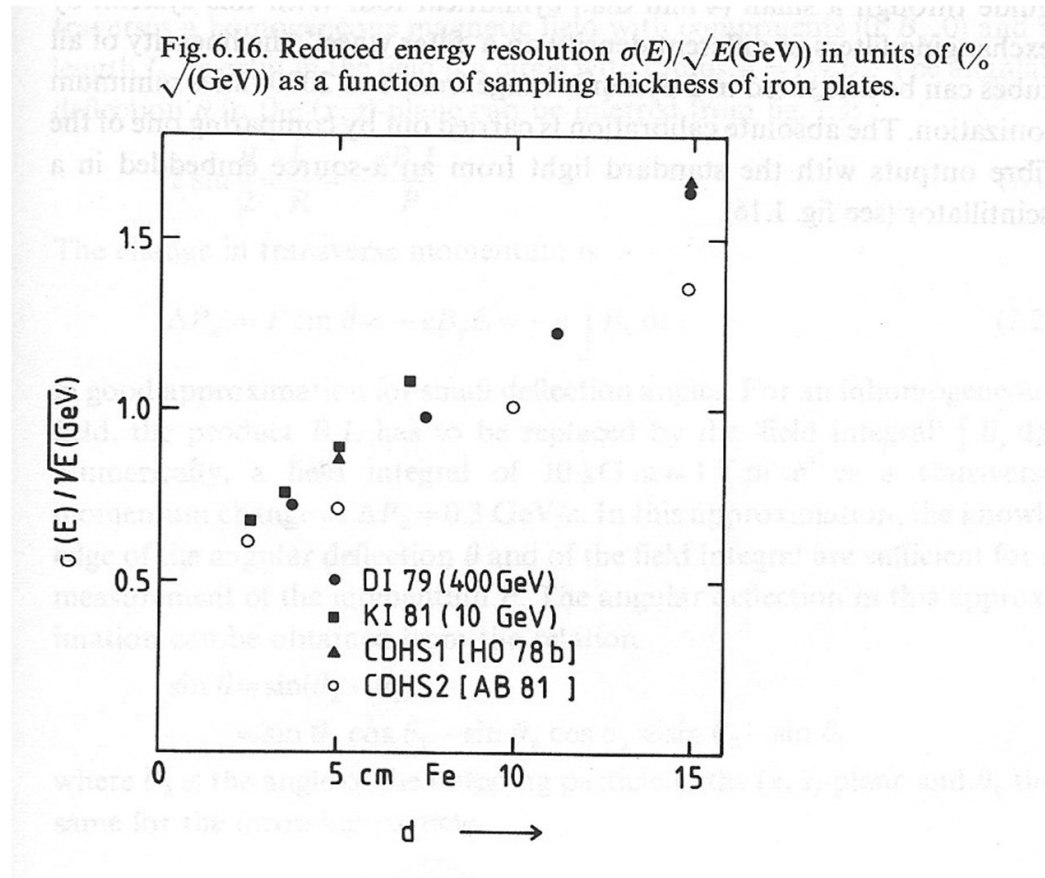


Energy resolution

Fig. 6.13. Relative energy resolution $\sigma(E)/E$ for different calorimeters; Fe (1.5 mm) and U (1.7 mm) from [FA 77]; Fe (25 mm) from [AB 81, BL 82].



Dependence of resolution on sampling characteristics



Technologies

Electromagnetic calorimeters

◆ Crystals

(current calorimeters) CsI (TI)	$2.3\%/\sqrt[4]{E} \oplus 1.9\%$	<i>BaBar</i>
	$1.5\%/\sqrt[4]{E} \oplus 1.2\%$	<i>BELLE</i>
PbWO₄	$2.8\%/\sqrt{E} \oplus 0.6\%$	<i>CMS</i>
	$3.3\%/\sqrt{E}$ (low noise term)	<i>ALICE</i>

◆ *LAr/Pb* (accordion)

$$10\%/\sqrt{E} \oplus 0.7\% \quad \text{ATLAS}$$

◆ *Scint./Pb* (shashlik)

$$10\%/\sqrt{E} \oplus 1\% \quad \text{LHCb}$$

Technologies

Hadron Calorimeters

◆ *Scint. / Brass* $\sim 100\% \sqrt{E} \oplus 4.5\%$ CMS
(WLS readout)

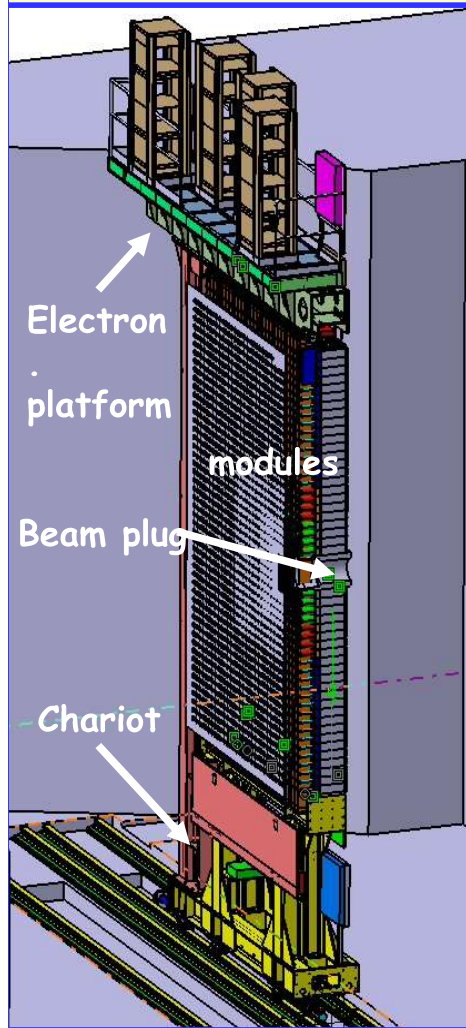
◆ *LAr / Brass* $\sim 60\% \sqrt{E} \oplus 3\%$ ATLAS (end-cap)

◆ *Scint / Fe (WLS readout)* $\sim 50\% \sqrt{E} \oplus 3\%$ ATLAS (barrel)
(tiles oriented parallel to the beam)

◆ *Scint / Fe (WLS readout)* $\sim 70\% \sqrt{E} \oplus 10\%$ LHCb
(similar to ATLAS tile calorimeter,
but planar geometry, 5.4λ depth)

*not compensated calorimeters
optimization of the jet energy resolution important !*

Two halves on chariots
and electronics platform
on top

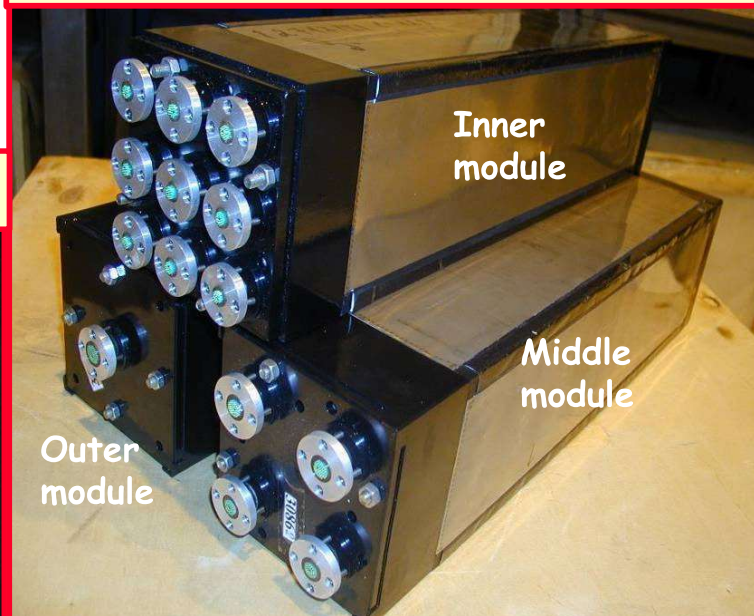


Overview
of LHCb ECAL

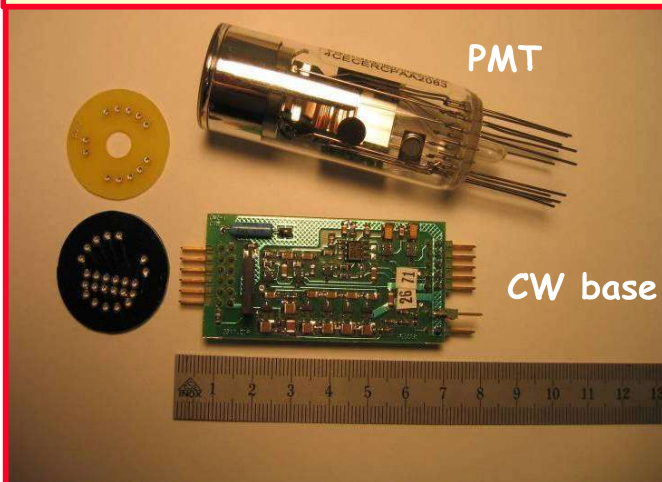
Fibres with loops



3312 shashlik modules with



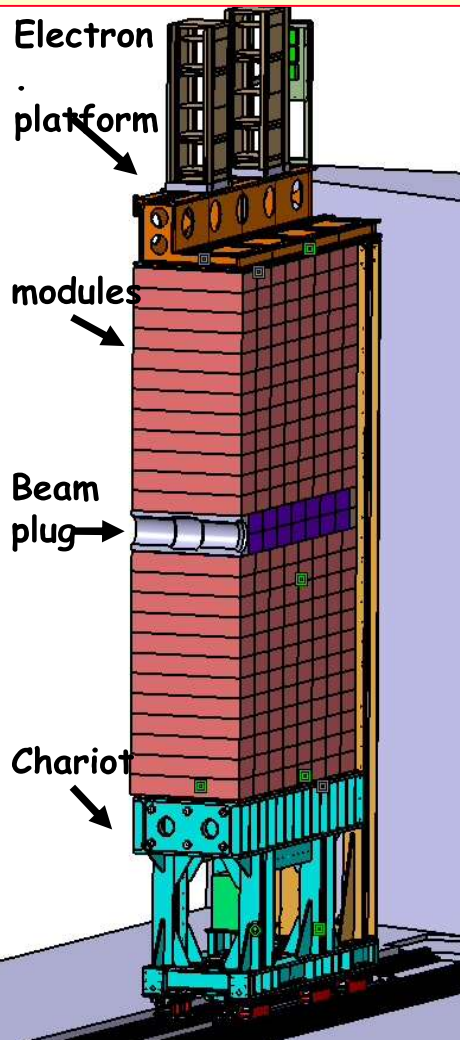
PMT and CW base



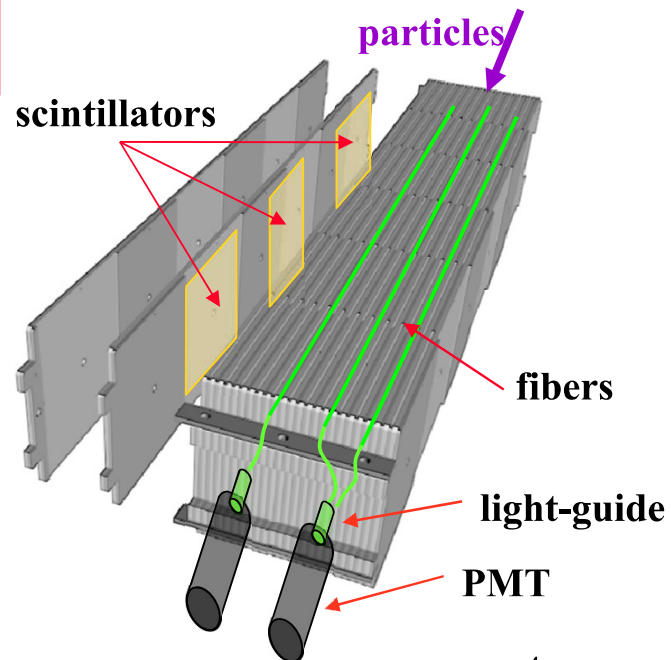
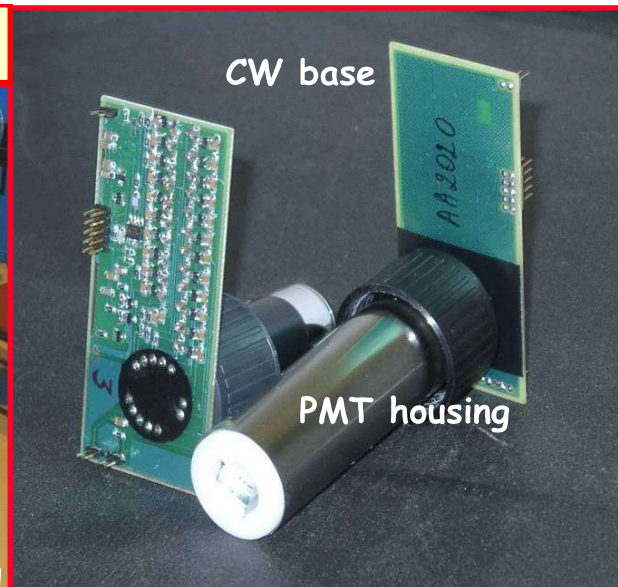
Scintillators, lead-



Overview of LHCb HCAL

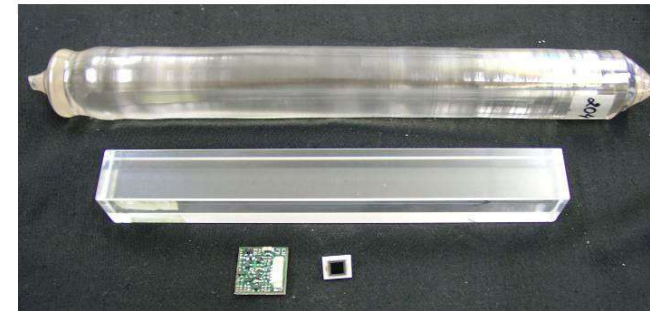
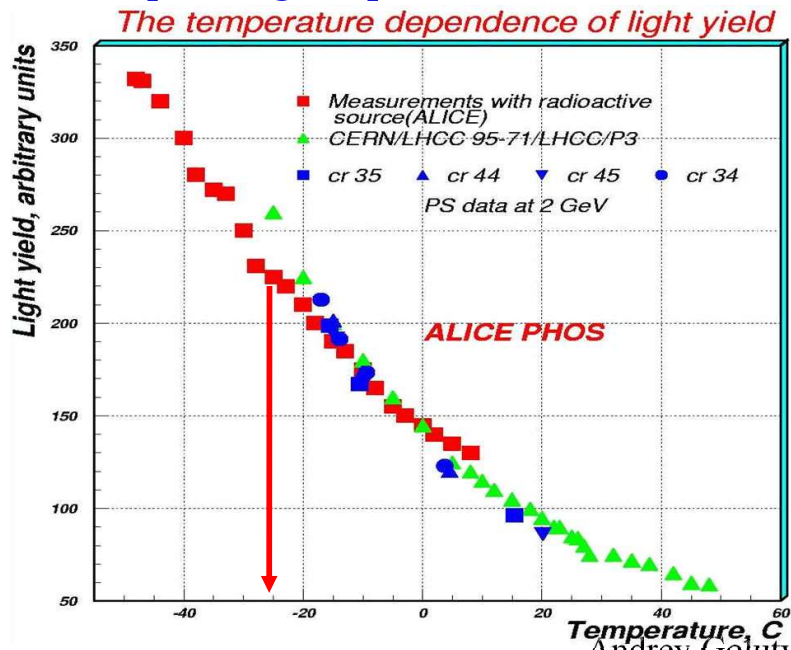
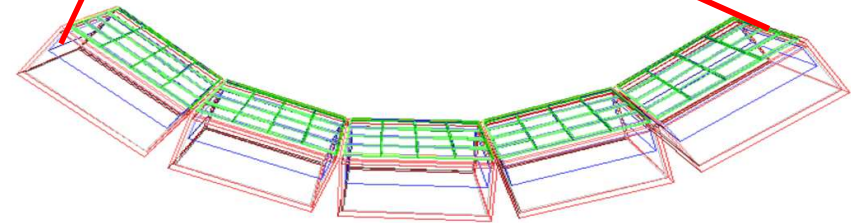


52 modules with longitudinal tiles



ALICE PHOS electromagnetic calorimeter

- 17920 PWO crystals
- distance to IP: 4.6m
- coverage in pseudo-rapidity:
 $|\Delta\eta| < 0.12$
- coverage in azimuthal angle:
 $\Delta\Phi < 100^\circ$
- crystal size: $22 \times 22 \times 180 \text{ mm}^3$
- Depth : $20X_0$
- photo readout: APD + CSP
- operating temperature: -25°C

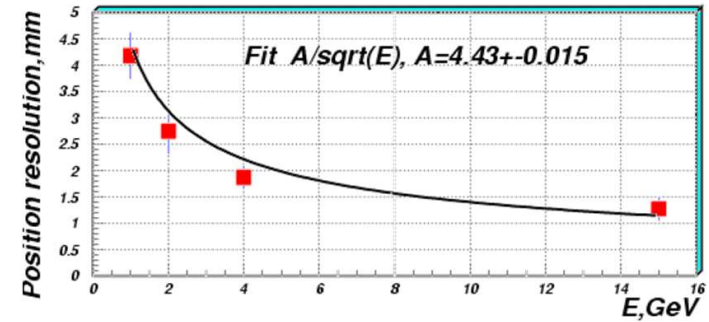
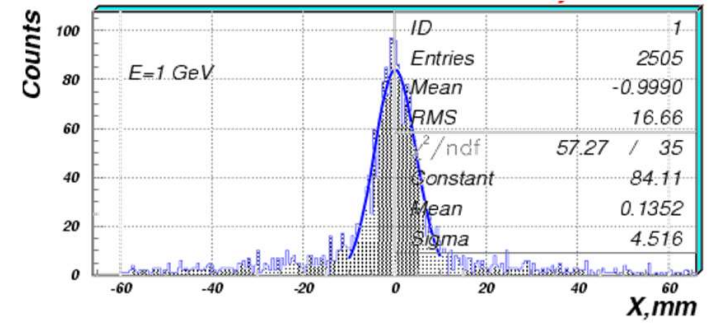
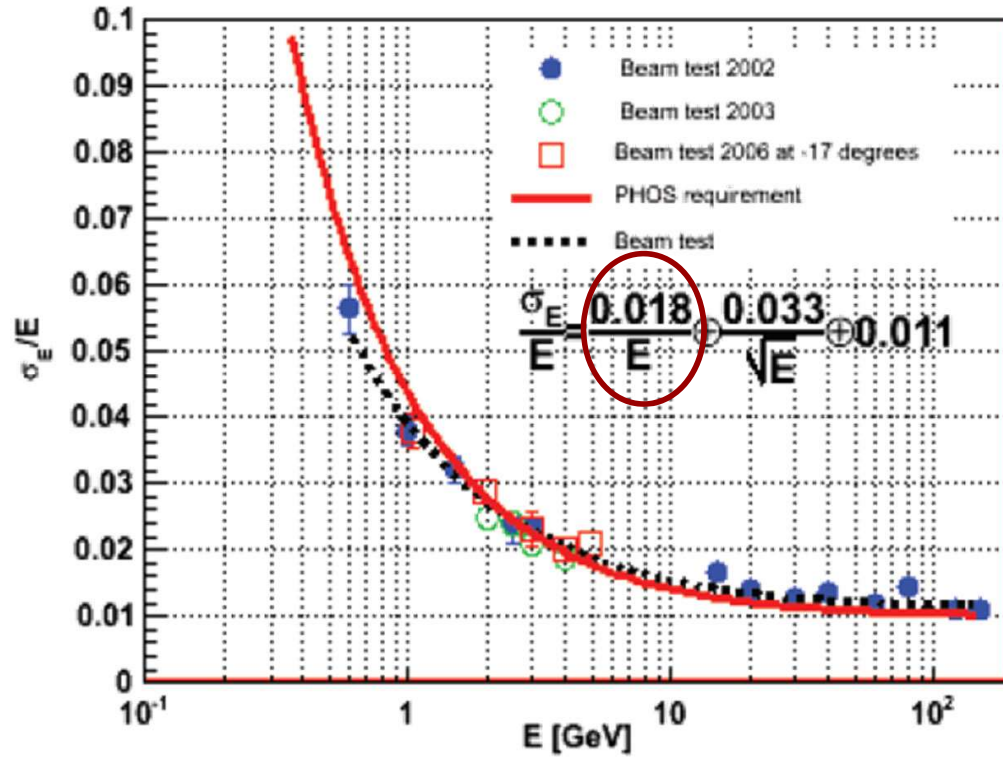


Andrey Golutvin

VCI 2007

PHOS: energy and position resolution

(Daicu Zhou at QM2006)



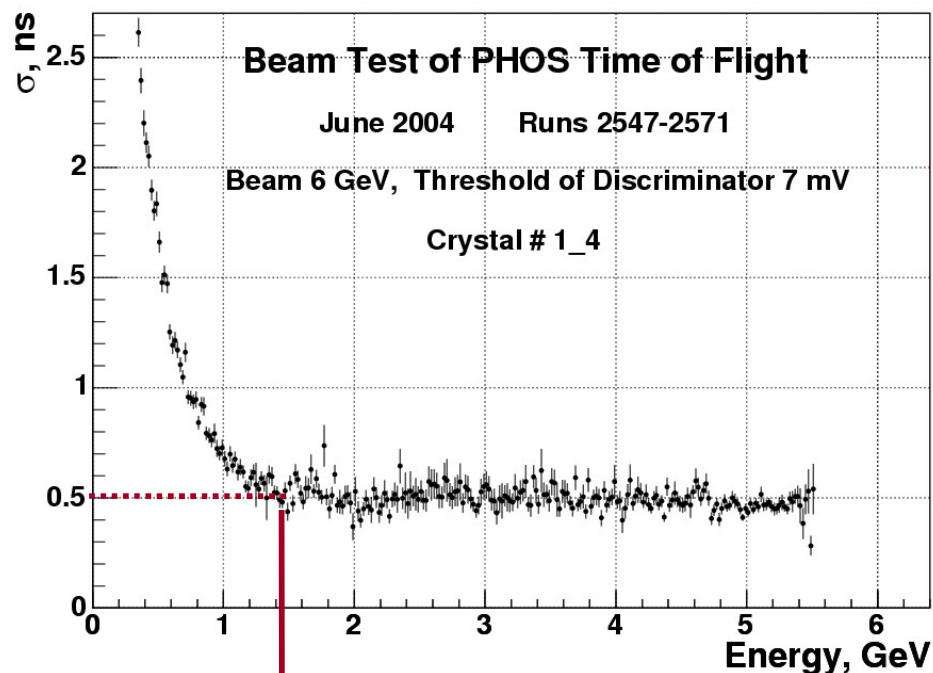
$\langle \sigma_x \rangle \sim 2.7 \text{ mm @ } 2 \text{ GeV}$

$\langle \sigma(E)/E \rangle \sim 3\%$, $\sigma(\sigma(E)/E) \sim 0.1\% \text{ @ } 2 \text{ GeV}$

PHOS: timing and mass resolution

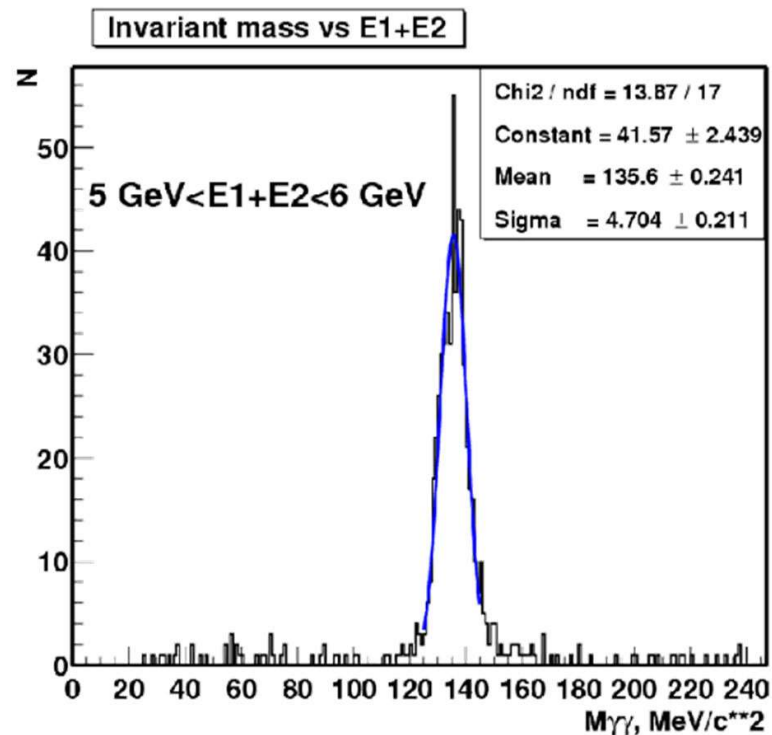
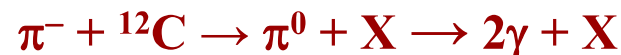
(Daicu Zhou at QM2006)

Timing resolution measurement with the electron beam. Standard start-stop method with an external trigger



$\sigma \sim 0.5$ ns at $E > 1.5$ GeV

Invariant mass spect

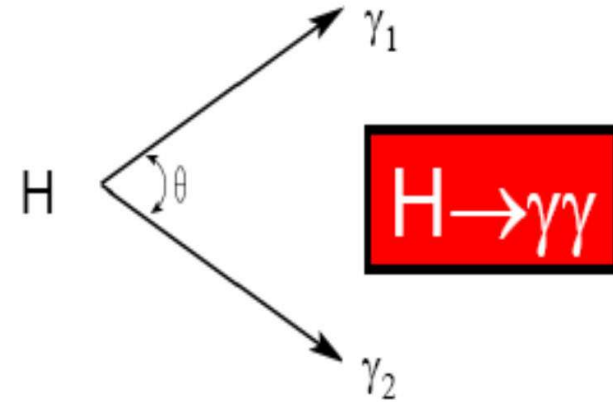
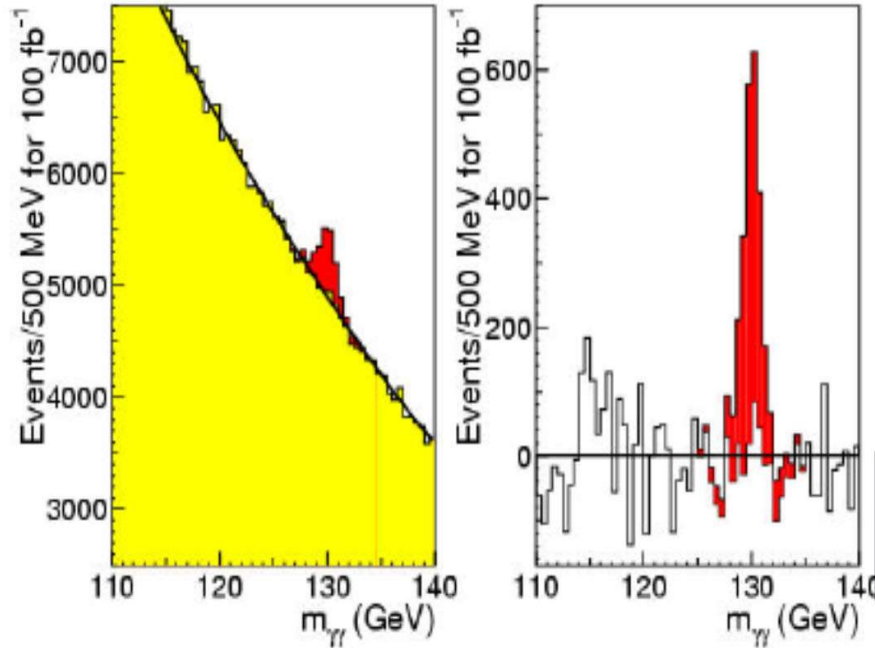


$\sigma(\pi^0) = 4.7$ MeV/c^2

π^0 is hard to see in ion-ion collisions

→ potential problem for intercalibration with data

Physics requirements (ATLAS/CMS)



$$\sigma m / m = 0.5 [\sigma E_1 / E_1 \oplus \sigma E_2 / E_2 \oplus \sigma \theta / \tan(\theta/2)],$$

where $\sigma E / E = a / \sqrt{E} \oplus b \oplus c/E$ and E in GeV

CMS: $\Delta\theta$ relies on interaction vertex measurement

ATLAS: $\Delta\theta$ possible with calorimeter alone

Similar for ATLAS and CMS

Electromagnetic calorimetry

- *Excellent energy resolution from 10 GeV to 300 GeV
($H \rightarrow \gamma\gamma$, $H \rightarrow 4e$)*
- *Good e/jet and γ/jet (particularly γ/π^0) separation*

Hadron calorimetry

- *Measurement of energy and direction of jets and missing transverse energy flow ($|\eta|$ up to 5)*